東京大学 大学院新領域創成科学研究科
基盤科学研究系
先端エネルギー工学専攻

平成 24 年度

修士論文

Filamentary plasma formation modeling in cm-scale millimeter wave fields at atmospheric pressure

－　大気圧下で cm スケールのミリ波領域に生成される フィラメント型プラズマのモデル化　－

2013 年 2 月提出
指導教員　小紫　公也　教授

47116076　武市　天聖

Contents

1. Introduction 4

1.1 Microwave Rocket 4

1.1.1 Discharge phenomenon in Microwave Rocket 4

1.1.2 Experimental observation 7

1.2 Objective 10

2. Numerical Analysis of the Millimeter-wave discharge 12

2.1 Theory of modeling millimeter wave discharge 12

2.2 Modeling physics 15

2.2.1 Microwave and Maxwell's equation 15

2.2.2 Fluid models for plasma 16

2.2.3 Introduction of quasineutral assumption and effective diffusion 21

2.3 Numerical method 25

2.3.1 FDTD (Finite Difference Time Domain) scheme for electromagnetic field 25

2.3.2 Formulation of the quasineutral plasma equation 31

2.3.3 Coupling Maxwell's equations with plasma model 34

2.3.4 Source term modeling 36

3. Results and discussion 40

3.1 Calculation conditions 40

3.2 Plasma formation in the domain to which E vector is perpendicular 43

3.3 Plasma formation in the domain to which H vector is perpendicular 47

3.4 The velocity of the plasma front 51

3.4.1 Modifying of ν_i and ν_a for Tokyo University experiments 51

3.4.2 Ionization front propagation in our experimental power region 54

3.4.3 Ionization front propagation in our experimental power region.....56

3.4.4 Discussion.....58

4. Conclusions.....60

Acknowledgement

I thank everyone who helped me and supported me to complete this thesis.

First I would like to appreciate my advisor, Professor Kimiya Komurasaki. He has given me a lot of opportunities and helpful advice. I would like to express my thanks to Professor Yoshihiro Arakwa, for giving me advice to improve my study. I would like to also say appreciation to Associate Professor Hiroyuki Koizumi for his sound advice.

I'm also grateful to Dr. Keishi Sakamoto and Dr. Oda(Japan Atomic Energy Agency) for giving opportunities for using the supercomputer at JAEA. Without any of these supports, this thesis would not have been completed. Thank you.

Gratitude is also extended to the following members in our research group, Mr Toshikazu Yamaguchi, Mr Masafumi Fukunari, Mr Shohei Saitoh, Mr Anthony Arnault, Mr Kenta Asai and Mr Satoshi Kurita.

Also thanks to all Doctoral people for giving me fruitful advice.

I also wish to thank all other members in Arakawa-Komurasaki-Koizumi laboratory.

Finally, I give my special thanks to my family throughout my education.

1. Introduction

1.1 Microwave Rocket

Microwave Rocket is one of the Beamed Energy Propulsion systems applicable to future space launches. Propulsive energy is repetitively supplied by pulsed microwave beams irradiated form the ground and the atmospheric air is used as a propellant, so that it can be propelled without any energy sources or propellants onboard. In addition, it does not require complicated structures like combustion chambers and turbo pump systems equipped on conventional liquid rocket engines. Therefore, it is expected to achieve a high payload ratio and a low launch cost [1].

Microwave Rocket consists of a cylindrical tube and a reflector for ignition. The closed end of the cylindrical tube has a conical reflector called “a thrust wall” and has inlet of the microwave beam, in which air is exhausted and refilled through. Its thrust generation mechanism is explained in the analogy of the pulse detonation engine (PDE) model, which is based on propagation of the detonation wave in a tube shaped engine. The detonation wave is driven by ionization front propagation into wave source. So, in the energy conversion process, it is very important to understand the mechanism of ionization front propagation. Thus, for clarifying the mechanism, it becomes important to know the propagation structure of ionization front in microwave discharge of the rocket, especially plasma formation process in a filamentary form in atmospheric pressure.

1.1.1 Discharge phenomenon in Microwave Rocket

High power millimeter-wave discharge in atmospheric air is characterized by filamentary structure and a supersonic propagation of the ionization front into wave source, driving a shockwave.

The filamentary structure has some characteristics, especially in high enough gas pressure as described below.

In the past studies [2], this filamentary structure is remarkable in high pressure. When the pressure is decreased, one can observe the transitions from a well-defined array of filaments to a smeared-out array, and finally to a diffuse plasma. This tendency agreed with our past experiments as shown in Figure 1-1.

Figure 1-1 Millimeter wave discharge in high and low pressure

The below figures show pictures of plasma patterns taken in the (***E***, ***k***) plane (***E*** is the electric field, ***k*** is the wave vector) and (***H***, ***k***) plane (***H*** is the magnetic field) of incident wave during the propagation of the plasma array toward the wave source. We can see from these figures, the structure are different between in the (***E***, ***k***) plane and (***H***, ***k***) plane. The experiments of [2-4] shows the formation of plasma filaments that aligned the electric filed (in (***E***, ***k***) plane). The distance between filaments is on the order of $\lambda/4$, where λ is the wave-length of the incident electromagnetic field.

Above characteristics of discharge propagation remained as in the case of linear polarization. The below figures show the plasma filaments in circular polarized wave. We can see from these figures, the ionization wave propagated into wave source in a spiral form. The step and diameter of the spiral were of order $\lambda/4$ [5].

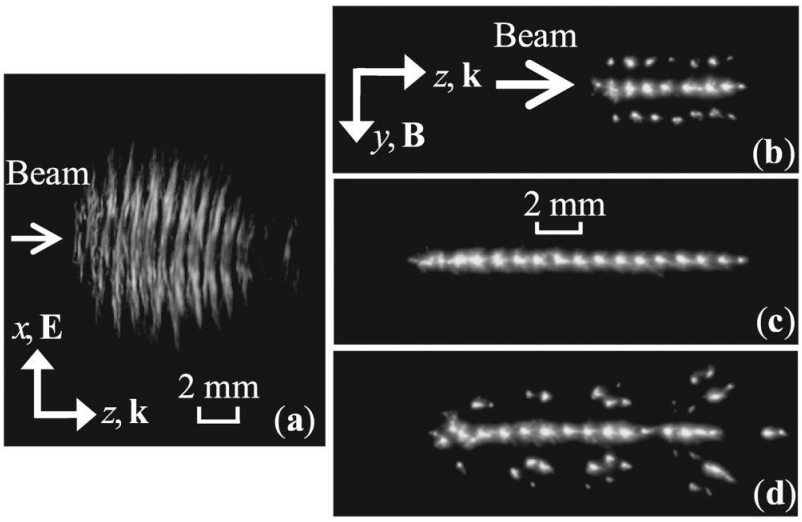

Figure 1-2 Typical time-integrated image volume breakdown plasma image in (a) *E* plane and (b)-(d) *H* plane (camera exposure time >> pulse width)-Microwave 1 MW 110 GHz [3]

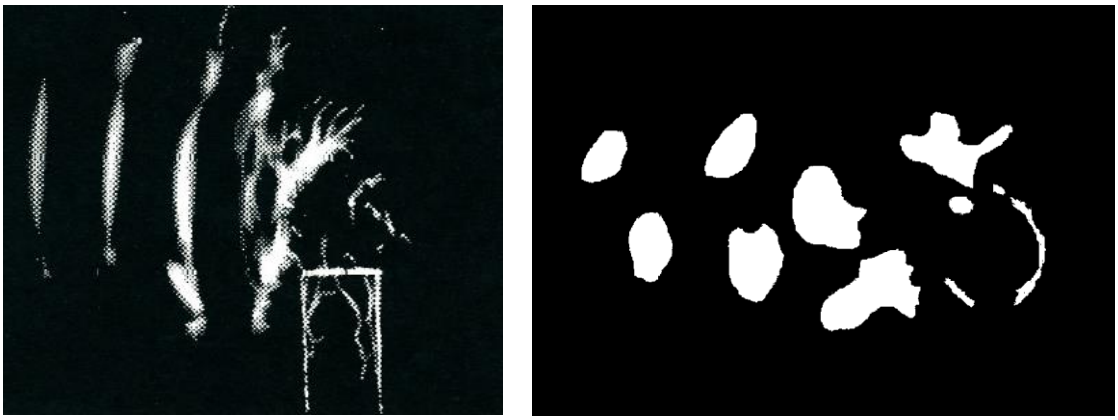

Figure 1-3 Typical time-integrated image volume breakdown plasma image in (a) *E* plane and *H* plane (camera exposure time >> pulse width)-Microwave 300-400 kW 7 GHz [4]

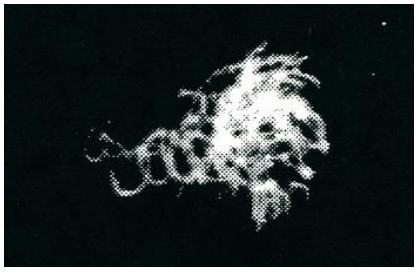

Figure 1-4 Typical time-integrated image volume breakdown plasma image in circular polarized wave [5]

1.1.2 Experimental observation

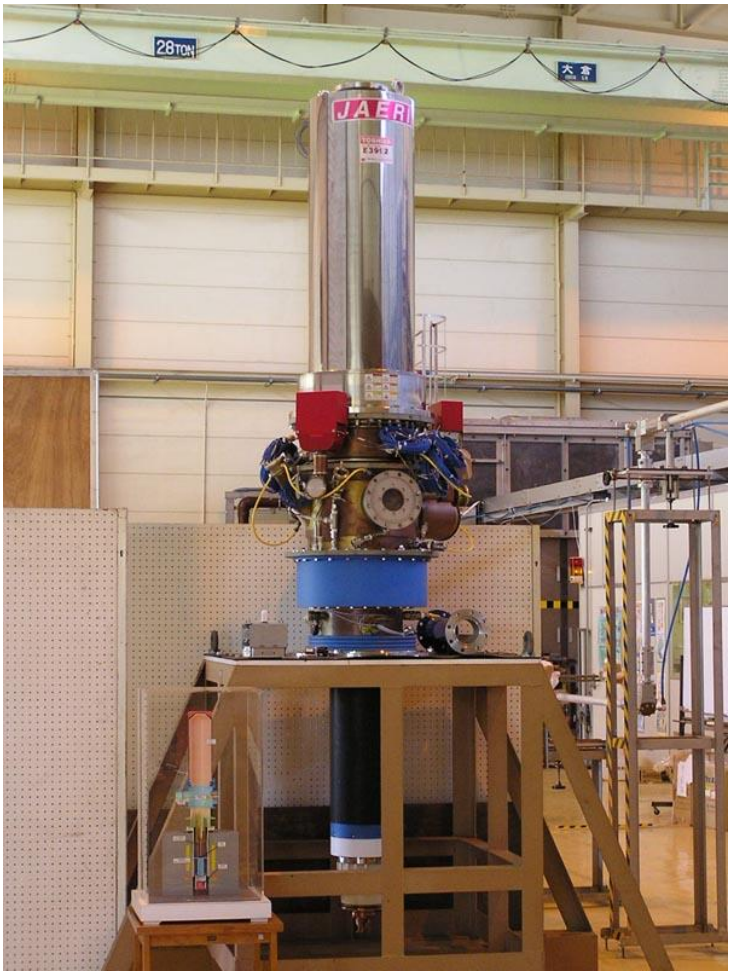

Figure 1-5 Gyrotron

As of 2002, the experiments performed at JAEA showed the formation of regular self-organized filamentary plasma arrays structure and the ionization front propagation toward the microwave source along with the development of Microwave Rocket. A 1MW-class 170GHz gyrotron was used as a microwave generator. It was developed at Japan Atomic Energy Agency (JAEA) for Electron Cyclotron Heating and Current Drive (ECH&CD) in International Thermonuclear Experimental Reactor (ITER). Its specifications are listed in Table 1. It has achieved 60% energy conversion efficiency from electricity with Single-stage Depressed Collector (SDC) as an energy recovery system. The millimeter wave was trans-

mitted through corrugated waveguides, and the profile of the output millimeter wave beam was a fundamental Gaussian beam with 20.4mm radial beam waist.

Table 1-1 Gyrotron's specification

Parameters	Values
Microwave Frequency	170GHz
Output Power	< 1MW
Pulse Duration	0.1ms to 1000s
Beam Profile	Gaussian
Beam Diameter	40mm
Electrical Efficiency	50-60%

Figure 1-6 is the schematic of the discharge experiments. Two kinds of camera were applied, one was used for capturing the open-shutter (time integrated) images in the entire discharge event and another one was the fast intensified camera, which can see the snapshots of the discharge state at a certain stage. The working gases in the experiments were mainly air at atmospheric pressure.

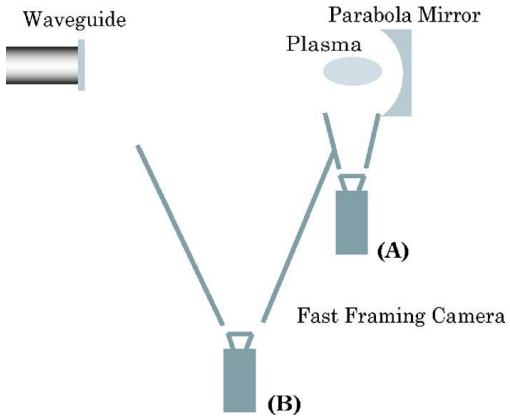

Figure 1-6 Our experimental apparatus of plasma observation [6]

In our filamentary plasma, the discharge was initiated at t=0. Figure 1-7 at t=0 shows that the ignition occurs in atmospheric air near the focal point.

The subsequent photographs show, the ionization front propagated in three directions. They are classifiable into two types: a branch on the left-hand side and two spokes on the right-hand side. The left branch absorbs the millimeter-wave beam power provided from the waveguide directly during the pulse duration, grows to a large branch and propagated into wave source. On the other hand, two small spokes absorb the millimeter wave reflected on the parabolic reflector.

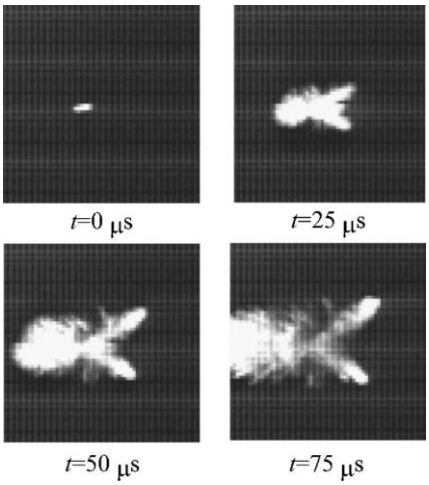

Figure 1-7 Photograph of ionization front propagation [6]

Figure 1-8 shows the time-integrated image of our ionization front propagation. The right hand side of figure 1-8 shows the trace of ionization in the edge region.

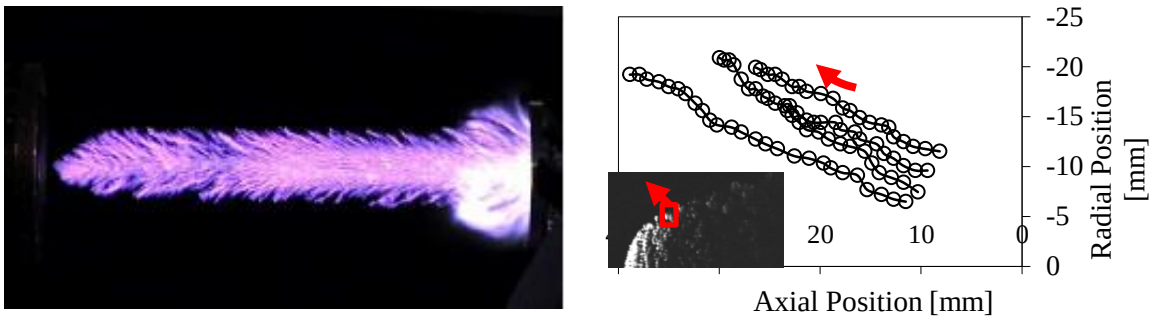

Figure 1-8 Typical image of ionization front (open exposure), Trace of ionization front (in the edge)

We can see from these figures, our ionization front propagation is characterized by granular plasmoids propagating not along or perpendicular to the electric field, but obliquely to the field in the edge region. However around the center region, the plasma pattern is not clear. Hence, this leads to one of the motivations for conducting the numerical simulation.

1.2 Objective

The detailed understanding of the mechanisms leading to the plasma dynamics and formation of complex filamentary structures after microwave breakdown at high pressure is very important to evaluate the potential applications of microwave plasmas. Of course, this will inevitably lead to the development of Microwave Rocket. But, the plasma dynamics is less well understood.

In this thesis work we try to establish a numerical model for the millimeter-wave discharge at high (atmospheric) pressure with clear physical concepts. The model is described in chapter 2. The numerical model is based on a simple quasi-neutral fluid model for the plasma with reference to Boeuf's model [7]. The diffusion in this model is an effective diffusion with a parameter that describes the transition from free diffusion at the plasma edge to ambipolar diffusion inside the plasma bulk. The microwave is described with Maxwell's equations. In addition, the ionization and attachment frequency in this model are effective in any beam power density. The numerical scheme for plasma equation and the finite-difference-time-domain(FDTD) scheme, as well as the absorbing boundary condition (or outgoing boundary condition) proposed by Mur [8]. The ionization and attachment frequencies are supposed to depend on the reduced effective field and the plasma density variations are averaged over one cycle of the microwave. By this coupling and these modeling, it will be possible to reproduce the local filed enhancement by wave interaction and discharge in the field.

Thus, as a first step, 2-dimensional numerical analysis was conducted to see if this modeling can reproduce our experimental filamentary plasma. In dozens of times the size of plasma element scale, the steady plasma structure formation was simulated, and we conducted the comparison of simulation results with previous experimental results.

Accordingly, from the simulation and the comparison, my objective is to clarify the mechanism of plasma formation which leads to the enhancement of efficiency of Microwave Rocket.

2. Numerical Analysis of the Millimeter-wave discharge

2.1 Theory of modeling millimeter wave discharge [32]

The plasma column formed in atmospheric air by a millimeter wave beam is shown in Figure 2-1, which shows side-view photographs of the discharge development. As this figure shows, the ionization front propagates towards the upstream of the millimeter-wave beam source.

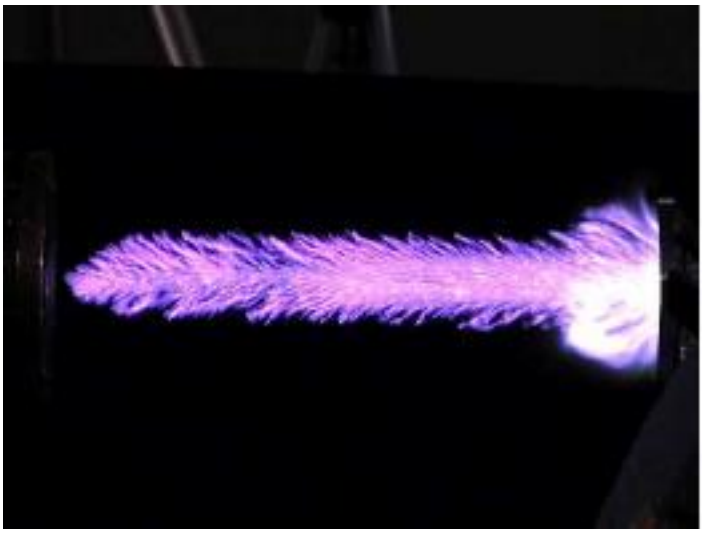

Figure 2-1 Photograph of Microwave Plasma, 700kW, τ=0.4msec

In a microwave discharge, the primary ionization of the gas due to the electron motion is the only production mechanism that controls breakdown. Breakdown occurs when the gain in electron density due to the ionization of the gas becomes greater than the loss of electrons by diffusion, attachment to neutral molecules, and recombination with positive ions.

In the past studies, the studies of plasma dynamics for microwave discharge were generally based on a continuity equation, and this idea was kept in almost all the following modeling works. The density equation is considered over time scales larger than the micro-

wave cycle and can be considered as integrated over a period of the microwave field so that only diffusion (no drift tern) appears in the continuity equation as shown in the below equation.

$$\frac{\partial n}{\partial t} = (\nu_i - \nu_a)n + \Delta(Dn) - r_{ei}n^2 \qquad (2\text{-}1)$$

where n is the electron density, ν_i is the ionization frequency, ν_a is the frequency of attachment of electrons to neutral molecules, D is the electron diffusion coefficient, and r_{ei} is the electron-positive ion recombination coefficient.

At the ignition stage of microwave rocket, electron density is relatively small and the plasma and dimension is also smaller than Debye length $\lambda_D = (\varepsilon_0 kT_e/e^2 n)^{1/2}$, the diffusion in equation (2-1) is an electron free diffusion D_e. Once the electron density reaches a value such that the dimension of the plasma is no longer smaller than the plasma Debye length, the electrons no longer diffuse freely, and the equation above becomes the ambipolar diffusion coefficient D_a in equation (2-1).

Actually, there is no clear consensus in the literatures, on what kind of diffusion coefficient should be used in equation (2-1). Although there is unquestionable that ambipolar diffusion should be used in the plasma bulk when the plasma dimension is large with respect to the minimum Debye length, the local Debye length becomes very large at the plasma edge, since the plasma density goes to zero there, thus electrons should diffuse freely at the edge. Mayhan *et al*. [9], citing the work of Allis and Rose's [10] (which was related to ambipolar to free transition near the walls of a plasma column) describe the diffusion transition in microwave breakdown with the expression:

$$D_s = D_e \frac{1 + 0.036\xi}{1 + 7.2\xi} \qquad (2\text{-}2)$$

with $\xi = \Lambda^2 ne/\varepsilon_0 kT_e$, and $\mathbf{\Lambda}$ is the local characteristics diffusion length, which is a common concept in the cavity discharge. Equation (2-2) was used to describe the transition from global

free diffusion to global ambipolar diffusion during the growth of the electron density in a microwave field. Our concern, mentioned above, is that even if diffusion is ambipolar in the plasma bulk, it should be free at the plasma edge where the local Debye length goes to infinity.

More recently, Nam and Verboncoeur [11] used an ambipolar diffusion coefficient in their simulation of microwave breakdown in the similar conditions of the MIT experiments [2, 3], but their calculated plasma densities seemed unrealistically large.

Maxwell's equations in the form (2-3), (2-4) or the derived wave equation are used to describe the microwave with impact of the plasma (the plasma is coupled to the field through the conduction or electron current term $\boldsymbol{J}_c$). In theoretical analyses the wave equation can be solved in the same time step with the plasma model. But with Maxwell's equations (2-3) and (2-4) the interaction between microwave and plasma can be seen more clearly.

$$\nabla \times \boldsymbol{H} = \varepsilon \frac{\partial \boldsymbol{E}}{\partial t} + \boldsymbol{J}_e \tag{2-3}$$

$$\nabla \times \boldsymbol{E} = -\mu_e \frac{\partial \boldsymbol{H}}{\partial t} \tag{2-4}$$

As said above, the plasma model is coupled to Maxwell's equations through the conduction current in equation (2-5) for more clear reproduction of experiments. As the ion current is much smaller with respect to the electron current, thus the conduction current in Maxwell's equations becomes mostly the electron current.

$$\boldsymbol{J}_e = -en\boldsymbol{u} \tag{2-5}$$

where the electron mean velocity $\boldsymbol{u}$ is obtained from the simplified electron momentum transfer equation given by

$$\frac{\partial \boldsymbol{u}}{\partial t} = -\frac{e}{m}\left(\boldsymbol{E} + \boldsymbol{u} \times \boldsymbol{B}\right) - \nu_m \boldsymbol{u} \tag{2-6}$$

with ν_m is the momentum transfer collision frequency between electrons and neutral molecules.

2.2 Modeling physics

2.2.1 Microwave and Maxwell's equation

Electromagnetic waves can be classified according to the wavelengths (or frequencies). The band of the wavelengths ranges from as long as 1 m to as short as1 mm (or with frequencies from 200 MHz to 200GHz).

Maxwell's equations are a set of four equations, which firstly appeared throughout J. C. Maxwell. Maxwell's equations are the basis of macroscopic electromagnetic theory, which is the most basic and important theory for analyzing electromagnetic problems. Maxwell's equations can be written in many forms. Here, we present the basic differential time domain form in a linear isotropic medium:

$$\nabla \times \boldsymbol{H} = e\frac{\partial \boldsymbol{E}}{\partial t} + \boldsymbol{J}_e \tag{2-7}$$

$$\nabla \times \boldsymbol{E} = -\mu\frac{\partial \boldsymbol{H}}{\partial t} \tag{2-8}$$

$$\nabla \cdot (\varepsilon \boldsymbol{E}) = \rho \tag{2-9}$$

$$\nabla \cdot (\mu \boldsymbol{H}) = 0 \tag{2-10}$$

where, $\varepsilon = \varepsilon_r\varepsilon_0$, $\mu = \mu_r\mu_0$, $\varepsilon_0$and μ_0 are permittivity and permeability of free space, ε_r and μ_r are relative values of permittivity and permeability for a specific linear isotropic medium respectively, for free space and air the values of ε_r and μ_r can be considered as one.

The first equation (2-7) is total current equations, it is Ampère's circuital law with Maxwell's bound current correction, the second (2-8) is Maxwell-Faraday equation derived from Faraday's law of induction, (2-9) and (2-10) are Gauss's law for electric field and magnetic field respectively. These four equations represent all the information needed for linear isotropic mediums to completely specify the electromagnetic behavior over time as long as the initial state is specified and satisfies the equations. Conveniently, the field and sources can be

set to zero at the initial time. The two divergence equations (2-9) and (2-10) are in fact redundant as they are included within the curl equations and the initial conditions.

2.2.2 Fluid models for plasma [32]

Models of the discharge should be built on a microscopic description of the particles in the discharge. However the discharge gas in this work is atmospheric air, which is a mixture with complex compositions (N_2, O_2, CO_2, Ar, etc.). It will be unnecessary work to describe the behaviors of every particle species in the discharge. Therefore we simply treat the ionized air as a mixture of one type of positive ions, electrons and neutral particles, and pursue a 'simple' model to describe the evolution of the discharge plasma.

All plasma models are founded in the Boltzmann equation. This equation results from the notion of a grand canonical ensemble, the Liouville equation, in statistical mechanics, and the assumption that the particle ensemble under consideration is sufficiently large to ensure that statistical fluctuations are small enough to be neglected.

The Boltzmann equation describes the evolution of the velocity distribution function $f(r, \boldsymbol{v}, t)$ of a single particle species, which gives the particle number of specific species per unit phase volume with velocity $\boldsymbol{v}$ at the location r and at time t. The general form of the Boltzmann equation reads:

$$\frac{\partial f}{\partial t} + \boldsymbol{v} \cdot \nabla f + \frac{\boldsymbol{F}}{m} \cdot \nabla_v f = \left(\frac{\partial f}{\partial t} \right)_e \qquad (2\text{-}11)$$

The left hands side reflects the flow of the particles in phase space, where m is the particle mass, $\boldsymbol{F}$ is the macroscopic forces (electro-magnetic and gravity forces) that cause the acceleration of the particles, while ∇_v indicates the gradient operator in velocity space. The right hands side of the equation $(\partial f / \partial t)_e$ denotes the effect of the microscopic, collisions and

radiation. Coupling with the multiple of Boltzmann equations for the different species together with their right hands side is necessary to describe a discharge. However, this seven-dimensional equation cannot be solved completely for any practical application at present, even for a single species.

In this thesis we are interested in fluid description, which is applicable to the conditions which the mean free path of particles is significantly smaller than the characteristic dimension of the plasma. In fluid models the behaviors of various discharged particle species are described in terms of average, macroscopic, hydrodynamic quantities such as particle density n, mean velocity $\boldsymbol{u}$, and mean energy ε. All those macroscopic quantities correspond to velocity moments of the distribution function $f(r, \boldsymbol{v}, t)$:

$$n(r,t) = \int f(r,\boldsymbol{v},t)d\boldsymbol{v} \tag{2-12}$$

$$\boldsymbol{u} = \langle \boldsymbol{v} \rangle = \frac{1}{n}\int \boldsymbol{v} f(r,\boldsymbol{v},t)d\boldsymbol{v} \tag{2-13}$$

$$\varepsilon = \frac{m}{2}\langle \boldsymbol{v}^2 \rangle = \frac{m}{2n}\int v^2 f(r,\boldsymbol{v},t)d\boldsymbol{v} \tag{2-14}$$

The fluid equations, describing the evolution of the macroscopic variables, can be obtained by taking different velocity moments of Boltzmann equation (2-11).

Multiplying Boltzmann equation by some function of velocity $\Phi(\boldsymbol{v})$ and integrating over all velocity components gives the transport equation for the average moment quantity given by

$$\langle \Phi(\boldsymbol{v}) \rangle = \frac{1}{n}\int \Phi(\boldsymbol{v}) f d\boldsymbol{v} \tag{2-15}$$

After some manipulating, equation (2-11) becomes the general transport equation for the macroscopic moment $\langle \Phi \rangle$,

$$\frac{\partial n\langle \Phi \rangle}{\partial t} + \nabla \cdot \left(n\langle \Phi \boldsymbol{v} \rangle \right) - \frac{n}{m}\langle \boldsymbol{F} \cdot \nabla_v \Phi \rangle = \left(\frac{\partial n\langle \Phi \rangle}{\partial t} \right)_e \tag{2-16}$$

where $\boldsymbol{F}$ is divergence free in velocity space, which holds true for the electromagnetic force and the right hands side describes the effect collisions.

This equation has the form of conservation equation for the density of the average or macroscopic quantity $\langle \Phi \rangle$. Now we are free to choose the velocity function Φ. As we can see, Φ=1 results in the particle continuity equation,

$$\frac{\partial n}{\partial t} + \nabla \cdot (n\boldsymbol{u}) = S\,, \tag{2-17}$$

where the source term S is the net number of charged particles created per unit time per unit volume due to collisions.

Setting Φ= m$\boldsymbol{v}$ yields the momentum conservation equation,

$$\frac{\partial n\boldsymbol{u}}{\partial t} + \nabla \cdot (n\boldsymbol{u}\boldsymbol{u}) = -\frac{1}{m}\nabla \cdot \boldsymbol{P} + n\frac{\boldsymbol{F}}{m} + R, \tag{2-18}$$

where $\boldsymbol{P} = m\int(\boldsymbol{v}-\boldsymbol{u})(\boldsymbol{v}-\boldsymbol{u})\, f\mathrm{d}\boldsymbol{v}$ is the pressure tensor, and $R = n\boldsymbol{u}\nu_m$ is the momentum source due to momentum transfer collisions with other species, with ν_m the macroscopic momentum transfer collision frequency.

And setting $\Phi = m|\boldsymbol{v}|^2/2$ gives the energy conservation equation,

$$\frac{\partial (n\varepsilon)}{\partial t} + \nabla \cdot (n\boldsymbol{u}\varepsilon + \boldsymbol{P}\cdot\boldsymbol{u} + \boldsymbol{Q}) = n\boldsymbol{u}\cdot\boldsymbol{F} + S_\varepsilon\,, \tag{2-19}$$

where $\boldsymbol{Q} = \int|\boldsymbol{v}-\boldsymbol{u}|^2(\boldsymbol{v}-\boldsymbol{u})\, f\mathrm{d}\boldsymbol{v}$ is the heat flux vector, S_ε is the energy gained or lost in collisions.

One crucial problem is that the equations obtained from (2-16) are not be able to completely solved as the n-th moment equation would introduce the (n+1)-th of macroscopic moment, which can be obviously see from the second term on the left hand side of the general transport equation (2-16), such that any finite set of moment equations would have more unknowns than number of equations. Therefore some additional information, limiting assumption or additional physical setting is necessary to obtain the result. The first standard approximation for plasma is to assume that pressure tensor is diagonal and isotropic:

$$\boldsymbol{P} = enT\boldsymbol{I} \tag{2-20}$$

Where $enT = \frac{m}{3}\int |\boldsymbol{v}-\boldsymbol{u}|^2 f d\boldsymbol{v}$ is the scalar pressure, T is the temperature in unit of eV, and $\boldsymbol{I}$ is the identity matrix. By substituting equations (2-17) and (2-20), the momentum conservation equation (2-18) becomes

$$\frac{\partial \boldsymbol{u}}{\partial t} + (\boldsymbol{u}\cdot\nabla)\boldsymbol{u} + \frac{e}{mn}\nabla(nT) = \frac{\boldsymbol{F}}{m} - \nu_m \boldsymbol{u} \tag{2-21}$$

For high collision condition, i.e., discharges at high pressure, the charged particle momentum equation can be further simplified by removing the inertia term and the magnetic term such that they are included in the force term on the right hand side. With respect to the collision term, assuming that collisions take place on much shorter time and smaller length scale than macroscopic field, pressure variations and cyclotron motion. With these assumptions the momentum conservation equation turns to be,

$$\boldsymbol{\Gamma} = n\boldsymbol{u} = \frac{q}{m\nu_m} n\boldsymbol{E} - \frac{e}{m\nu_m}\nabla(nT) \equiv \pm\mu n\boldsymbol{E} - \nabla(Dn) \tag{2-22}$$

where q is the particle charge.

This is the so-called drift-diffusion equation, and the two transport coefficients of mobility and diffusion:

$$\mu \equiv |q|/m\nu_m\,, \tag{2-23}$$

$$D \equiv eT/m\nu_m\,. \tag{2-24}$$

These will be different for each particle species, and these two coefficients are connected by the Einstein relation:

$$\frac{D}{\mu} \equiv \frac{e}{|q|}T\,. \tag{2-25}$$

By these definitions the continuity equation can be rewritten in a drift-diffusion form

$$\frac{\partial n}{\partial t} + \nabla\cdot\left(\pm\mu n\boldsymbol{E} - \nabla(Dn)\right) = S\,. \tag{2-26}$$

One of the main questions to close the fluid models is how to describe the source term in the equation, i.e., ionization, attachment and recombination. The most popular closure for collision condition is the local field approximation, assuming local equilibrium between electric acceleration, which are the energy gain from the electric field, the collision momentum and the energy losses, so that the ionization frequencies would depend only on the local electric field $\boldsymbol{E}$, or rather, the reduced electric field $\boldsymbol{E}/N$ (or $\boldsymbol{E}/p$) since the collision frequency is proportional to the gas density N (or pressure). Using the local field approximation the energy equation is not necessary anymore [15]. If we consider the ratio of diffusion coefficient and mobility to be constant, the diffusion coefficient in the equation above can be put out of ∇,

$$\frac{\partial n}{\partial t} + \nabla \cdot \left(\pm \mu n \boldsymbol{E} - D \nabla n \right) = S . \tag{2-27}$$

For charged particle in high frequency microwave field, Maxwell's and plasma equations are coupled with the conduction current density in the plasma, which generally reduces to the electron current density. The mean electron velocity for the electron current in high frequency fields is generally obtained from another approximation of the momentum equation (2-21). Assuming that the distance travelled over one field period is small with respect to the length scale of field and pressure variation, so all gradients can be neglected:

$$\frac{\partial \boldsymbol{u}}{\partial t} = \frac{q}{m} \left(\boldsymbol{E} + \boldsymbol{u} \times \boldsymbol{B} \right) - \nu_m \boldsymbol{u} . \tag{2-28}$$

This simplified form of the electron momentum equation is appropriate in the calculation of the electron current in Maxwell's equations in the condition that the time scale is much shorter than the microwave period. Also, equation (2-28) is an expression for conditions without magnetic field. If an external magnetic field is present and its effect is not negligible the corresponding magnetic force must be added in the right hands side of equation (2-28). The magnetic field of the wave itself must also be included in some specific cases and leads to

the so-called ponder motive effect. Moreover, in our cases, the simulation domain is relatively large (cm-scale), so we take into account the magnetic field.

2.2.3 Introduction of quasineutral assumption and effective diffusion [32]

In microwave discharge plasma, the electric field in equation (2-18) should be the sum of the microwave field and a DC or slowly varying space charge field. The wave field plays an essential role in electron heating and ionization, but its contribution to particle transport averaged over one wave cycle is negligible, so only space charge field contributes to charged particle transport, therefore equation (2-27) can be rewritten as,

$$\frac{\partial n}{\partial t} + \nabla \cdot \left(\pm \mu n \boldsymbol{E}_{sp} - D \nabla n \right) = S \tag{2-29}$$

where the space charge field is noted with $\boldsymbol{E}_{sp}$.

As mentioned before, we simply treat the ionized air in our problem as a mixture of positive ions, electrons and neutral particles. Two equations therefore are needed to describe the discharge plasma,

$$\frac{\partial n_e}{\partial t} + \nabla \cdot \left(\pm \mu_e n_e \boldsymbol{E}_{sp} - D_e \nabla n_e \right) = S\,, \tag{2-30}$$

$$\frac{\partial n_i}{\partial t} + \nabla \cdot \left(\pm \mu_i n_i \boldsymbol{E}_{sp} - D_i \nabla n_i \right) = S\,. \tag{2-31}$$

In microwave field with the absence of DC field, quasineutrality ($n_e = n_i = n$) is often a good approximation. With the quasineutral approximation, we can write $\boldsymbol{\Gamma}_i = \boldsymbol{\Gamma}_e = \boldsymbol{\Gamma}$, and can express the space charge (ambipolar) field as:

$$\boldsymbol{E}_{sp} = \frac{D_i - D_e}{\mu_e + \mu_i} \frac{\nabla n}{n}. \tag{2-32}$$

So the common flux is then given by

$$\boldsymbol{\Gamma} = \mu_i \frac{D_i - D_e}{\mu_i + \mu_e} \nabla n - D_i \nabla n = -\frac{\mu_e D_i + \mu_i D_e}{\mu_i + \mu_e} \nabla n\,. \tag{2-33}$$

Thus, equations (2-30) and (2-31) can be represented in a common form

$$\frac{\partial n}{\partial t} - \nabla \cdot (D_a \nabla n) = S \tag{2-34}$$

which is known as the ambipolar diffusion coefficient.

In most conditions, we can take $\mu_e \gg \mu_i$ and D_i is negligible with respect to D_e, so the magnitude of D_a can be estimated with

$$D_a \approx \frac{\mu_e}{\mu_i} D_e \tag{2-35}$$

The ambipolar diffusion coefficient above is obtained with the quasineutral assumption, which is valid in the bulk of static plasma, but for the plasma in open space even if the plasma dimension is much larger than the Debye length, the plasma density at the edge goes to zero and, therefore, there should be a small region in the edge where the electrons freely diffuse instead of ambipolarly. This question has been considered somewhat empirically in the literature. In our work, we use Boeuf *et al'*s [7] more theoretical modeling for this coefficient. The way of modeling is shown below.

Since free diffusion prevails only in the front while the plasma bulk is controlled by ambipolar diffusion, we need a parameter to describe this transition. We define below an effective diffusion coefficient, deduced from the current continuity equation in the drift diffusion approximation, to describe this transition. We start the derivation by considering the 'more exact' description for the ionized air without the quasineutral assumption, i.e., equations (2-30) and (2-31). The space charge electric field $\boldsymbol{E}_{sp}$ in the equations is related to the electric potential by $\boldsymbol{E}_{sp} = -\nabla\Phi$, and the electric potential can be obtained from Poisson's equation:

$$\nabla^2 \Phi = -\frac{e}{\varepsilon_0}(n_i - n_e). \tag{2-36}$$

Subtracting equation (2-30) from (2-31) yields:

$$\frac{\partial}{\partial t}(n_i - n_e) + \nabla \cdot \left[(\mu_i n_i - \mu_e n_e)\boldsymbol{E}_{sp} - (D_i \nabla n_i - D_e \nabla n_e)\right] = 0. \tag{2-37}$$

Eliminating densities in the first term with Poisson's equation and using the quasineutral approximation, we obtain

$$\tau_m \frac{\partial \boldsymbol{E}_{sp}}{\partial t} + \boldsymbol{E}_{sp} = \frac{D_i - D_e}{\mu_i + \mu_e} \frac{\nabla n}{n}, \tag{2-38}$$

where $\tau_m = \varepsilon_0/en(\mu_i+\mu_e)$ is the dielectric (or Maxwell) relaxation time. With respect to the ambipolar field (2-34) there is an extra time partial differential term on the left hands side of equation (2-38), and this is what we will play with.

The first term at the left hands side of equation (2-38) can be replaced by $\tau_m U_{\text{ion}} \nabla \boldsymbol{E}_{sp}$, where we use U_{ion} as the front propagates at the velocity $U_{\text{ion}} = 2\sqrt{v_i D_e}$. The velocity $U_{\text{ion}} = 2\sqrt{v_i D_e}$ can be seen in the some references [16, 17] as plasma streamer front propagation speed. $\nabla \boldsymbol{E}_{sp}$ in the front can be approximated with $\boldsymbol{E}_{sp}/2L$, where $L = \sqrt{D_e / v_i}$ is the characteristic length of the front. So, we get $\tau_m U_{\text{ion}} \nabla \boldsymbol{E}_{sp} \approx v_i \tau_m \boldsymbol{E}_{sp}$, which means the first term of equation (2-38) is of the order of $\alpha = v_i \tau_m$ with respect to second term.

Thus, equation (2-38) can be approximated with:

$$\boldsymbol{E}_{sp} = \frac{1}{1+\alpha} \frac{D_i - D_e}{\mu_i + \mu_e} \frac{\nabla n}{n}. \tag{2-39}$$

Using this space charge field expression, the electron flux turn to be (the second term of equation (2-30))

$$\boldsymbol{\Gamma}_e = -\left[\frac{1}{1+\alpha} \frac{D_i - D_e}{\mu_i + \mu_e} + D_e \right] \nabla n = -D_{eff} \nabla n, \tag{2-40}$$

with an effective diffusion coefficient

$$D_{eff} \approx \frac{\alpha D_e + D_a}{\alpha + 1}, \text{with } \alpha = v_i \tau_m \tag{2-41}$$

where we also used the assumption of $\mu_i \ll \mu_e$, $D_i \ll D_a$.

We can see from the above that the use of equation (2-34) has validity with the effective diffusion coefficient (2-40). Finally, we get the below equation,

$$\frac{\partial n}{\partial t} - \nabla \cdot \left(D_{eff} \nabla n \right) = S \qquad (2\text{-}42)$$

This model equation (2-40) is not mathematically exact but gives the good limits and a correct estimation of the parameter a controlling the crossover from free diffusion in the front (α »1or >1) to ambipolar diffusion in the bulk for electrons.

2.3 Numerical method

The numerical method is a way of discrete equations for the physical model, in which the partial differential terms are replaced by finite-differences or some other discrete schemes. Choosing an appropriate scheme is very important during the numerical simulations. In our works, we used Bouef's numerical scheme [7, 18] as a guide for our scheme.

2.3.1 FDTD (Finite Difference Time Domain) scheme for electromagnetic field

The FDTD method, first proposed by Yee in 1966 [19], is the most popular numerical method for the solution of electromagnetic problems. In the FDTD method the electric field (***E***) is defined on a grid that is offset both spatially and temporally from the magnetic field (***H***) grid. The fields at the next time step are deduced from the previous fields using a simple leap frog scheme.

2.3.1.1 FDTD Algorithm

In FDTD method, equations (2-3) and (2-4) are replaced by six coupled scalar equations in the3D rectangular coordinate system (*x*, *y*, *z*):

$$\begin{cases} \dfrac{\partial E_x}{\partial t} = \dfrac{1}{\varepsilon_0}\left(\dfrac{\partial H_z}{\partial y} - \dfrac{\partial H_y}{\partial z}\right) - \dfrac{1}{\varepsilon_0} J_x \\ \dfrac{\partial E_y}{\partial t} = \dfrac{1}{\varepsilon_0}\left(\dfrac{\partial H_x}{\partial z} - \dfrac{\partial H_z}{\partial x}\right) - \dfrac{1}{\varepsilon_0} J_y \\ \dfrac{\partial E_z}{\partial t} = \dfrac{1}{\varepsilon_0}\left(\dfrac{\partial H_y}{\partial x} - \dfrac{\partial H_x}{\partial y}\right) - \dfrac{1}{\varepsilon_0} J_z \end{cases} \tag{2-43}$$

$$\begin{cases} \dfrac{\partial H_x}{\partial t} = -\dfrac{1}{\mu_0}\left(\dfrac{\partial E_z}{\partial y} - \dfrac{\partial E_y}{\partial z}\right) \\ \dfrac{\partial H_y}{\partial t} = -\dfrac{1}{\mu_0}\left(\dfrac{\partial E_x}{\partial z} - \dfrac{\partial E_z}{\partial x}\right) \\ \dfrac{\partial H_z}{\partial t} = -\dfrac{1}{\mu_0}\left(\dfrac{\partial E_y}{\partial x} - \dfrac{\partial E_x}{\partial y}\right) \end{cases} \tag{2-44}$$

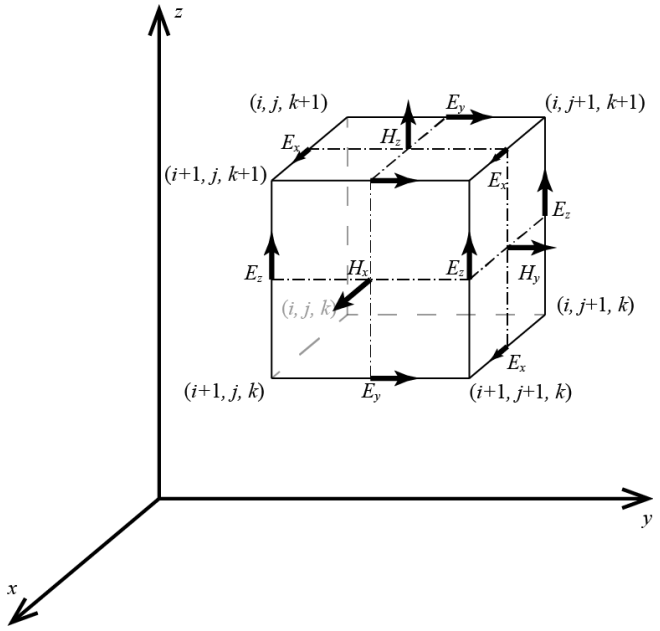

Figure 2-2 Positions of field components in a unit cell of the FDTD [19]

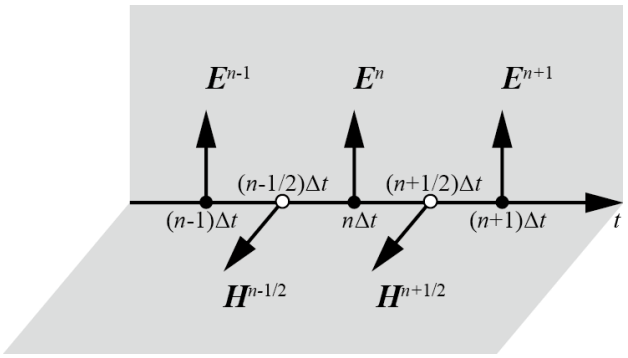

Figure 2-3 Positions of time components in a unit cell of the FDTD

Figure 2-3 is the illustration of Yee's FDTD lattice, this algorithm centers ***E*** and ***H*** components in 3D space so that every ***E*** component is surrounded by four circulating ***H*** components, and every ***H*** component is also surrounded by four circulating ***E*** components ; in time the ***E*** and ***H*** are centered in a leapfrog arrangement. Using the finite-difference notation and Yee's lattice, scalar Maxwell's equations (2-43) and (2-44), can be numerically approximated by

$$\begin{cases} \dfrac{E_x\big|_{i,j,k}^{n+1} - E_x\big|_{i,j,k}^{n}}{\Delta t} = \dfrac{1}{\varepsilon_0}\left(\dfrac{H_z\big|_{i,j+1/2,k}^{n+1/2} - H_z\big|_{i,j-1/2,k}^{n+1/2}}{\Delta y} - \dfrac{H_y\big|_{i,j,k+1/2}^{n+1/2} - H_y\big|_{i,j,k-1/2}^{n+1/2}}{\Delta z} - J_x\big|_{i,j,k}^{n+1/2} \right) \\ \dfrac{E_y\big|_{i,j,k}^{n+1} - E_y\big|_{i,j,k}^{n}}{\Delta t} = \dfrac{1}{\varepsilon_0}\left(\dfrac{H_x\big|_{i,j,k+1/2}^{n+1/2} - H_x\big|_{i,j,k-1/2}^{n+1/2}}{\Delta z} - \dfrac{H_z\big|_{i+1/2,j,k}^{n+1/2} - H_z\big|_{i-1/2,j,k}^{n+1/2}}{\Delta x} - J_y\big|_{i,j,k}^{n+1/2} \right) \\ \dfrac{E_z\big|_{i,j,k}^{n+1} - E_z\big|_{i,j,k}^{n}}{\Delta t} = \dfrac{1}{\varepsilon_0}\left(\dfrac{H_y\big|_{i+1/2,j,k}^{n+1/2} - H_y\big|_{i-1/2,j,k}^{n+1/2}}{\Delta x} - \dfrac{H_x\big|_{i,j+1/2,k}^{n+1/2} - H_x\big|_{i,j-1/2,k}^{n+1/2}}{\Delta y} - J_z\big|_{i,j,k}^{n+1/2} \right) \end{cases}, \quad (2\text{-}45)$$

$$\begin{cases} \dfrac{H_x\big|_{i,j+1/2,k}^{n+1/2} - H_x\big|_{i,j+1/2,k}^{n-1/2}}{\Delta t} = -\dfrac{1}{\mu_0}\left(\dfrac{E_z\big|_{i,j+1,k}^{n} - E_z\big|_{i,j,k}^{n}}{\Delta y} - \dfrac{E_y\big|_{i,j,k+1}^{n} - E_y\big|_{i,j,k}^{n}}{\Delta z} \right) \\ \dfrac{H_y\big|_{i,j,k+1/2}^{n+1/2} - H_y\big|_{i,j,k+1/2}^{n-1/2}}{\Delta t} = -\dfrac{1}{\mu_0}\left(\dfrac{E_x\big|_{i,j,k+1}^{n} - E_x\big|_{i,j,k}^{n}}{\Delta z} - \dfrac{E_z\big|_{i+1,j,k}^{n} - E_z\big|_{i,j,k}^{n}}{\Delta x} \right) \\ \dfrac{H_z\big|_{i+1/2,j,k}^{n+1/2} - H_z\big|_{i+1/2,j,k}^{n-1/2}}{\Delta t} = -\dfrac{1}{\mu_0}\left(\dfrac{E_y\big|_{i+1,j,k}^{n} - E_y\big|_{i,j,k}^{n}}{\Delta x} - \dfrac{E_x\big|_{i,j+1,k}^{n} - E_x\big|_{i,j,k}^{n}}{\Delta y} \right) \end{cases}. \quad (2\text{-}46)$$

As shown in (2-45) and (2-46) Yee's algorithm is second order accurate in both space and time. The fundamental constraint for Yee's cell is that the size must be much less than the wavelength for which accurate results are desired. And an often quoted constraint is "10 cells per wavelength"[20], meaning that the size of the cells should be $\lambda/10$ or less, which is much smaller than the Nyquist sampling limit ($\Delta x \leq \lambda/2$). So it is reasonable to say that a cell size of $\lambda/50$ can give a desired accuracy in most conditions. For the free space computational stability of equations (2-45) and (2-46) requires the courant condition as shown in below.

$$\Delta t \le \frac{1}{c_0\sqrt{\frac{1}{(\Delta x)^2}+\frac{1}{(\Delta y)^2}+\frac{1}{(\Delta z)^2}}} \tag{2-47}$$

$c_0 = (\varepsilon_0\mu_0)^{-1/2}$ denotes the speed of light in free space, and if $\Delta s = \Delta x = \Delta y = \Delta z$, the stability condition simplifies to $\Delta t \le \Delta s/c_0\sqrt{3}$.

For 2D problems, in which assuming source and materials have a translation symmetry, say, *z*-direction, the electromagnetic field quantities will be independent of the *z* coordinate, thus *z* derivation terms in Maxwell's equations become zero ($\frac{\partial}{\partial z}=0$). Then the full set of Maxwell's scalar equations in rectangular coordinates given by (2-43) and (2-44) reduces to

$$\begin{cases} \dfrac{\partial E_x}{\partial t} = \dfrac{1}{\varepsilon_0}\dfrac{\partial H_z}{\partial y} - \dfrac{1}{\varepsilon_0}J_x \\ \dfrac{\partial E_y}{\partial t} = \dfrac{1}{\varepsilon_0}\dfrac{\partial H_z}{\partial x} - \dfrac{1}{\varepsilon_0}J_y \\ \dfrac{\partial E_z}{\partial t} = \dfrac{1}{\varepsilon_0}\left(\dfrac{\partial H_y}{\partial x} - \dfrac{\partial H_x}{\partial y}\right) - \dfrac{1}{\varepsilon_0}J_z \end{cases} \text{ and } \begin{cases} \dfrac{\partial H_x}{\partial t} = -\dfrac{1}{\mu_0}\dfrac{\partial E_z}{\partial y} \\ \dfrac{\partial H_y}{\partial t} = \dfrac{1}{\mu_0}\dfrac{\partial E_z}{\partial x} \\ \dfrac{\partial H_z}{\partial t} = -\dfrac{1}{\mu_0}\left(\dfrac{\partial E_y}{\partial x} - \dfrac{\partial E_x}{\partial y}\right) \end{cases}. \tag{2-48}$$

For singular electromagnetic modes Maxwell's scalar equations can be further simplified, such as for transverse magnetic (TM) mode, ***E*** field only has the component in wave vector (***k***) direction and ***H*** field has components only in the transverse directions, and the finite difference scheme, given by (2-45) and (2-46) also can be simplified respectively. As in 2D problem only a single plane in the lattice, seen in Figure 2-3, is used and the stability condition turns to be $\Delta t \le \Delta s/c_0\sqrt{2}$, when $\Delta s = \Delta x = \Delta y$.

The Maxwell's equations (2-3) and (2-4) can be discretized to obtain a total field FDTD scheme as (2-45) and (2-46). Alternately the fields can be expressed separately as [20]

$$\boldsymbol{E} = \boldsymbol{E}_t = \boldsymbol{E}_i + \boldsymbol{E}_s, \tag{2-49}$$

$$\boldsymbol{H} = \boldsymbol{H}_t = \boldsymbol{H}_i + \boldsymbol{H}_s, \tag{2-50}$$

with subscripts *t*, *i*, and *s* for the total, incident, and scattered fields.

For a microwave discharge phenomenon, the separation expression allows further insight into the interaction process because microwave incident field can be easily written in a simple formula.

By the separate expression (2-49) and (2-50), Maxwell's equations can be rewritten as

$$\nabla \times (\boldsymbol{H}_i + \boldsymbol{H}_s) = \varepsilon \frac{\partial (\boldsymbol{E}_i + \boldsymbol{E}_s)}{\partial t} + \boldsymbol{J}_c(\boldsymbol{E}_t), \tag{2-51}$$

$$\nabla \times (\boldsymbol{E}_i + \boldsymbol{E}_s) = -\mu \frac{\partial (\boldsymbol{H}_i + \boldsymbol{H}_s)}{\partial t}. \tag{2-52}$$

As the incident and scattered fields must satisfy the Maxwell's equation independently in linear materials, so the incident fields traversing the media satisfy free space conditions

$$\nabla \times \boldsymbol{H}_i = \varepsilon_0 \frac{\partial \boldsymbol{E}_i}{\partial t}, \tag{2-53}$$

$$\nabla \times \boldsymbol{E}_i = -\mu_0 \frac{\partial \boldsymbol{H}_i}{\partial t}. \tag{2-54}$$

Subtracting the incident fields above from (2-53) and (2-54), we can obtain the equations governing the scattered fields

$$\nabla \times \boldsymbol{H}_s = \varepsilon_0 \frac{\partial \boldsymbol{E}_s}{\partial t} + (\varepsilon - \varepsilon_0) \frac{\partial \boldsymbol{E}_i}{\partial t} + \boldsymbol{J}_c(\boldsymbol{E}_t), \tag{2-55}$$

$$\nabla \times \boldsymbol{E}_s = -\mu_0 \frac{\partial \boldsymbol{H}_s}{\partial t} - (\mu - \mu_0) \frac{\partial \boldsymbol{H}_i}{\partial t}. \tag{2-56}$$

As the incident field can be specified analytically, we just need to approximate (2-55) and (2-56) with the numerical scheme of (2-45) and (2-46).

2.3.1.2 Absorbing conditions [8]

For problems in free space, it is impossible to set the simulation domain to be infinity or big enough to neglect the boundary effects, an Absorbing Boundary Condition (ABC) should be used to truncate the computational domain since the tangential components of the electric field along the outer boundary of the computational domain cannot be updated using the basic Yee's algorithm. The most popular two kinds of ABCs are those that derived from differential

equations and those that employ a material absorber [21, 22]. Differential-based ABCs are generally obtained by factoring the wave equation, and by allowing a solution which permits only outgoing waves, while the material-based ABCs employ an absorbing medium to dampen the propagating fields.

In this work, we use a differential-based ABC, which was proposed by G. Mur, to truncate the computational domain.

Eliminating $\boldsymbol{H}$ or $\boldsymbol{E}$ from Maxwell's equations for free space, we obtain

$$\left(\nabla^2 - \frac{1}{c_0^2}\frac{\partial^2}{\partial t^2}\right)\boldsymbol{W} = 0, \tag{2-57}$$

where $\boldsymbol{W}$ standing for $\boldsymbol{E}$ or $\boldsymbol{H}$. Thus,

$$\left(\nabla - \frac{1}{c_0}\frac{\partial}{\partial t}\right)\left(\nabla + \frac{1}{c_0}\frac{\partial}{\partial t}\right)\boldsymbol{W} = 0. \tag{2-58}$$

Above equation's left term indicates the wave is traveling in the direction of decreasing x if x=0 is boundary as shown in Figure 2-5.

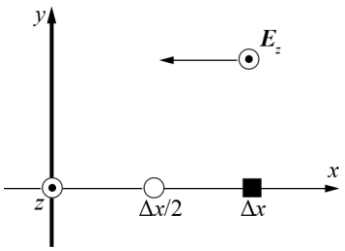

Figure 2-4 Plane wave incidence to absorbing boundary

In x=0, we formulate the equation (2-58) on the basis of FDTD. Then after some steps, the first order Mur's boundary condition is obtained as (2-59):

$$E_{z(0,j,k)}^{n+1} = E_{z(1,j,k)}^{n} + \frac{c_0\Delta t - \Delta s}{c_0\Delta t + \Delta s}\left(E_{z(1,j,k)}^{n+1} - E_{z(0,j,k)}^{n}\right). \tag{2-59}$$

In a similar way, the boundary condition approximations for the boundary plane of $x = x_d$ can be obtained, and also for the other boundary planes.

2.3.2 Formulation of the quasineutral plasma equation

The quasineutral plasma equation (2-42) can be solved with a explicit scheme for the diffusion and ionization terms, in order to impose the positivity of the solution the loss terms are treated implicitly or semi-implicitly.

$$n_{e(i,j,k)}^{n+1} = \frac{1}{1+\Delta t_p\left(\nu_a + r_{ei} n_{e(i,j,k)}^{n}\right)} \times \left\{ n_{e(i,j,k)}^{n}\left[1+\Delta t_p \nu_i\right] + D_{eff} \times \left[\frac{n_{e(i+1,j,k)}^{n} + n_{e(i-1,j,k)}^{n} - 2n_{e(i,j,k)}^{n}}{\Delta^2 x_p} + \frac{n_{e(i,j+1,k)}^{n} + n_{e(i\,j-1,,k)}^{n} - 2n_{e(i,j,k)}^{n}}{\Delta^2 y_p} + \frac{n_{e(i,j,k+1)}^{n} + n_{e(i\,j,,k-1)}^{n} - 2n_{e(i,j,k)}^{n}}{\Delta^2 z_p} \right] \right\} \tag{2-60}$$

where Δt and Δs_p, Δx_p, Δy_p, Δz_p note the time and space step for plasma.

In order to ensure the stability of the numerical scheme for the quasineutral plasma equation, the time step (Δt_p) must satisfy the CFL condition:

$$\Delta t \le \frac{\left(\Delta s_p\right)^2}{\left(3D_{eff,\max}\right)} \tag{2-61}$$

where Δs_p is the fluid mesh size and $D_{eff,\max}$ corresponds to maximum value of effective diffusion coefficient. However, we don't have to care about the condition because the time step of FDTD is much shorter than that of fluid equation.

In the problem of microwave breakdown at high pressure, the space gradient of plasma density can be extremely large, and we will see in the following chapters that the plasma equation (2-42) asks finer grid spacing than the FDTD grid for the Maxwell's equations. The density gradient can be estimated by characteristic length $\sqrt{D/\nu_i}$. For our condition (E_0 ~ a few hundred kV/m, p~760 torr), the diffusion coefficient is on the order of 10^{-3} m^2s^{-1} and the ionization frequency in the front is on the order of a few 10^7 s^{-1}, so that L of the front is in the

10 micrometer range, which is on the order of a few hundredths of the wavelength (1.73 mm for 170 GHz).

An efficient way to deal with the requirement of the finer grid to describe the sharp density gradients would be to apply an adaptive mesh refinement (AMR) scheme, symmetric boundary condition at center axis and an unequally-spaced mesh scheme.

First, about AMR scheme, it adapts the distribution of grids according to the density gradients. But it is very complex to apply the automatic AMR in our numerical model, and we found that using a fixed grid fine enough to resolve the density gradients led to reasonable computation times.

For example, we consider a double grid method, using different grid size for FDTD and plasma density. The ratio between two grid sizes is defined by

$$m = \Delta s / \Delta s_p \,. \tag{2-62}$$

where Δs is the grid spacing for the Maxwell equations (FDTD scheme) and Δs_p is for the fluid equation of the density.

Solutions of the quasineutral plasma equation need the transport coefficients, i.e., ionization frequency ν_i and attachment frequency ν_a, which are functions of the electric field. Since the electric field is available only at the coarser FDTD grid points, an interpolation is needed to obtain the electric field on the fine grid in order to estimate the ionization and attachment frequencies in the quasineutral plasma equation. For solving the equations on the fine grid, we will employ a simple bilinear interpolation scheme as shown in Figure 2-5 and the bilinear interpolation formula (2-62).

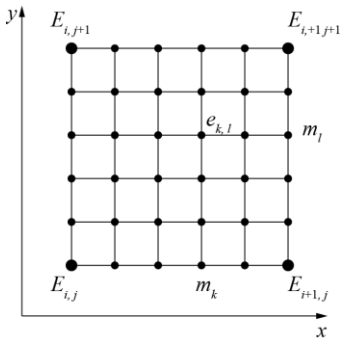

Figure 2-5 Overlapping coarse FDTD and fine density grid.

The values of the electric fields on the small pots can be obtained by the bilinear interpolation formula

$$e_{k,l} = \frac{(m-m_k)}{m}\frac{(m-m_l)}{m}E_{i,j} + \frac{m_k}{m}\frac{(m-m_l)}{m}E_{i+1,j} + \frac{(m-m_k)}{m}\frac{m_l}{m}E_{i,j+1} + \frac{m_k}{m}\frac{m_l}{m}E_{i+1,j+1}. \tag{2-63}$$

For reducing calculation cost, we introduce a symmetric boundary condition on the center plane. We set the condition x=0, z=0 plane. (Wave vector $\boldsymbol{k}$ is on the y axis.)

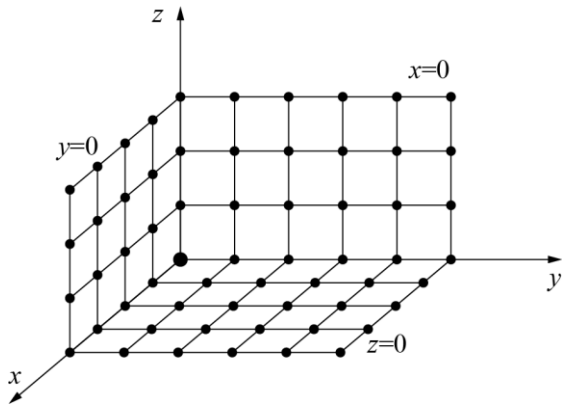

Figure 2-6 Schematic of calculation domain

Moreover, we introduce an unequally-spaced mesh scheme to solve much larger scale calculation domain. Figure 2-7 shows the schematic of the way of component's interpolation in the unequally-spaced mesh.

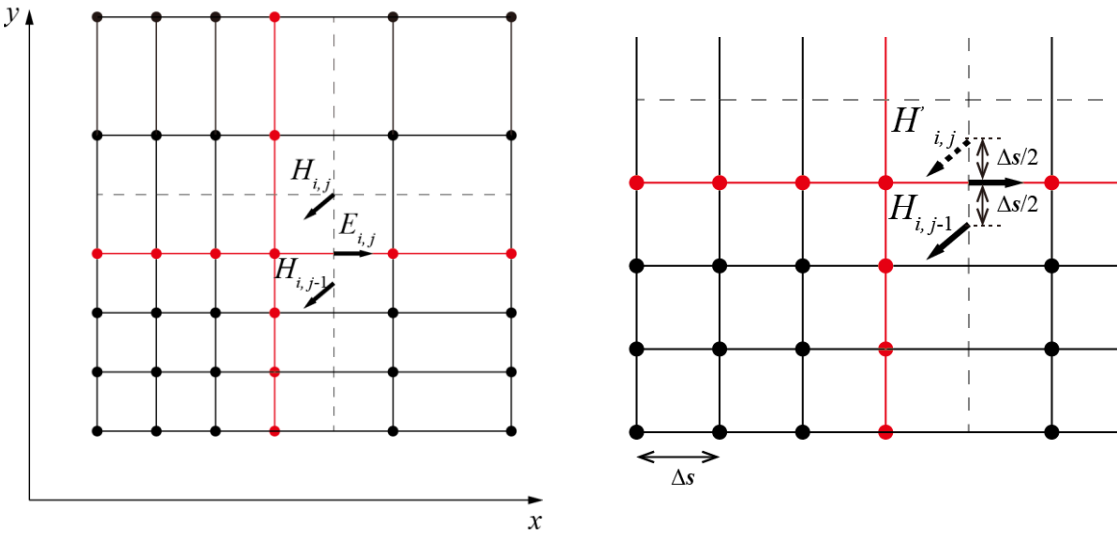

Figure 2-7 Non-uniform mesh

We use Jiang's modeling [23]. This modeling presents the FDTD method by using different mesh sizes of large ratio more than two. In this modeling, as shown in Figure 2-7, we have to interpolate the components on the boundary between different meshes (red axis in Figure 2-7).

2.3.3 Coupling Maxwell's equations with plasma model

As we discussed in the model section, the plasma due to the microwave discharge in atmospheric pressure can be treated as quasineutral, and equation (2-42) can give a good description for the evolution of the discharge plasma. In this section we describe the way how Maxwell's equations are numerically coupled with the plasma equations.

In gas discharge with local field approximation the apparent ionization frequency ν_i (including the attachment effect) depends on the local electric field only, or rather, the local reduced effective electric field. Also, the electron –ion recombination coefficient is supposed to be the function of the local electric field.

$$\frac{\partial n}{\partial t} - \nabla \cdot \left(D_{eff} \nabla n \right) = \nu_i n - r_{ew} n^2 \,, \tag{2-64}$$

$$\nabla \times \boldsymbol{H}_s = \varepsilon_0 \frac{\partial \boldsymbol{E}_s}{\partial t} + \left(\varepsilon - \varepsilon_0 \right) \frac{\partial \boldsymbol{E}_i}{\partial t} + \boldsymbol{J}_c \left(\boldsymbol{E}_t \right), \tag{2-65}$$

$$\nabla \times \boldsymbol{E}_s = -\mu_0 \frac{\partial \boldsymbol{H}_s}{\partial t}. \tag{2-66}$$

The conduction current $\boldsymbol{J}_c$ is approximated by the electron conduction current (the ion currents neglected because of the much smaller ion mobility):

$$\boldsymbol{J}_c\left(\boldsymbol{E}_t\right) = -en_e\boldsymbol{u}, \tag{2-67}$$

where $\boldsymbol{u}$ is the mean velocity of electrons, which can be obtain form the approximate momentum equation,

$$\frac{\partial \boldsymbol{u}}{\partial t} = -\frac{e}{m_e}\left(\boldsymbol{E}_t + \boldsymbol{u} \times \boldsymbol{B}_t\right) - \nu_m \boldsymbol{u}, \tag{2-68}$$

From equations (2-64) -(2-68), the quasineutral plasma model 'sees' Maxwell's equations through the conductive current, which depends both on the plasma density and the total electric field, and Maxwell's equations feedback with ionization (and attachment) frequency, which depends on the local reduced electric field under local field approximation.

The FDTD scheme in section is an explicit second order accurate time-domain method with centered finite differences. When a direct integration approximation is used for the electron momentum equation (2-68), writing [24, 25]

$$\frac{u^{n+1} - u^n}{\Delta t} + \nu_m \frac{u^{n+1} + u^n}{2} = -\frac{e}{m_e}\frac{E_t^{n+1} + E_t^n}{2}. \tag{2-69}$$

In the case of taking into account magnetic field effect, equation (2-69) can be rewritten as,

$$\frac{u^{n+1} - u^n}{\Delta t} + \nu_m \frac{u^{n+1} + u^n}{2} = -\frac{e}{2m_e}\left(E_t^{n+1} + E_t^n + \left(\nu_e^{n+1} + \nu_e^n\right) \times B_t^{n+\frac{1}{2}}\right). \tag{2-70}$$

a new leapfrog approximation can be made for equation (2-65) to improve the accuracy,

$$\begin{aligned} E_s^{n+1} = {} & E_s^n \frac{1-\beta}{1+\beta} + \frac{en\Delta t}{2\varepsilon_0}\frac{1+\alpha}{1+\beta}u^n - \frac{\beta}{1+\beta}\left(E_t^{n+1} + E_t^n\right) + \\ & \frac{\Delta t}{(1+\beta)\varepsilon_0}\nabla \times H_s^{n+\frac{1}{2}} - \frac{(\varepsilon - \varepsilon_0)/\varepsilon}{1+\beta}\left(E_t^{n+1} - E_t^n\right), \end{aligned} \tag{2-71}$$

$$u^{n+1} = \alpha u^n - \frac{e\Delta t}{2m_e\gamma}\left\{\left(E_t^{n+1} + E_t^n\right) + \left(u^{n+1} + u^n\right) \times \mu H_t^{n+\frac{1}{2}}\right\}, \qquad (2\text{-}72)$$

with $\alpha = \frac{1-a}{1+a}, \beta = \frac{\omega_p^2 \Delta t^2}{4\gamma} + \frac{\sigma \Delta t}{2\varepsilon}, \gamma = 1 + a, a = \frac{\nu_m \Delta t}{2}$.

where ω_p means the plasma angular frequency and σ is the electric conductivity of a medium.

2.3.4 Source term modeling

Now the remaining question is how the microwave field determines the ionization frequency. Generally, the ionization frequency can be found either by solving the kinetic equation for electron energy distribution or experimentally. The local field approximation mentioned above seems to be a reasonable approximation for the space dependence of the transport coefficients and collision frequencies. This approximation is made in most models of atmospheric discharges (e.g. DC steamer models). Under microwave conditions, by the dependence on the wave frequency and collision frequency, electron transport may or may not be in equilibrium with the local field at a given time. Thus we have to conduct modification of the modeling.

A usual approximation [26] is used when electron transport can be considered on time scales in the order of the field period. This gives an assumption that the electron transport coefficients and collision frequencies depend on the local value of an effective DC field that would give the same electron energy gain per unit-time as the microwave field, when this energy gain is integrated over one cycle. The average time for energy gain per unit-time is proportional to the average of the product of the electric field multiplied with the electron mean velocity. The calculation formula is written as follows $\langle -e\boldsymbol{E} \cdot \boldsymbol{v} \rangle$

The mean electron velocity is solution of the momentum equation (2-70) for a microwave field $\boldsymbol{E} = \boldsymbol{E}_0 \sin\omega t$, where E_0 is the amplitude, and can be written as

$$\boldsymbol{v} = \frac{e\boldsymbol{E}_0}{m_e\sqrt{\omega^2 + \nu_m^2}}\cos(\omega t + \varphi), \varphi = \arctan\frac{\nu_m}{\omega}, \tag{2-73}$$

so the mean energy gain per unit time that the field performs on an electron is

$$\left\langle -e\boldsymbol{E}\cdot\boldsymbol{v}\right\rangle_f = \frac{e^2E_0^2\nu_m}{2m_e\left(\omega^2 + \nu_m^2\right)}, \tag{2-74}$$

while mean energy gain in dc field is

$$\left\langle -e\boldsymbol{E}\cdot\boldsymbol{v}\right\rangle_{dc} = \frac{e^2E_{dc}^2}{m_e\nu_m}. \tag{2-75}$$

From (2-76) and (2-77), we can define an effective field,

$$E_{eff} = \frac{E_{rms}}{\sqrt{1+\omega^2/\nu_m^2}}. \tag{2-76}$$

where E_{rms} is the local root mean square field, which can be obtained from the FDTD over one cycle. So for high frequency conditions the transport coefficients and ionization frequency will be taken as a function of the local effective field defined by equation (2-76) using the same functional dependence as under a DC field.

One can easily find in the literature values of the ionization frequency in air as a function of the reduced electric field in the form of analytical expressions fitted from experiments or numerical simulations. However the range which experimental or simulation data exist is confined almost exclusively to indicated region I in Figure 2-8. Because it is not possible to ignite a self-sustained discharge without any initiated setting such as a metal rod or a preliminary discharge introduced by laser in II or III region, experiments under that conditions had not been conducted so much.

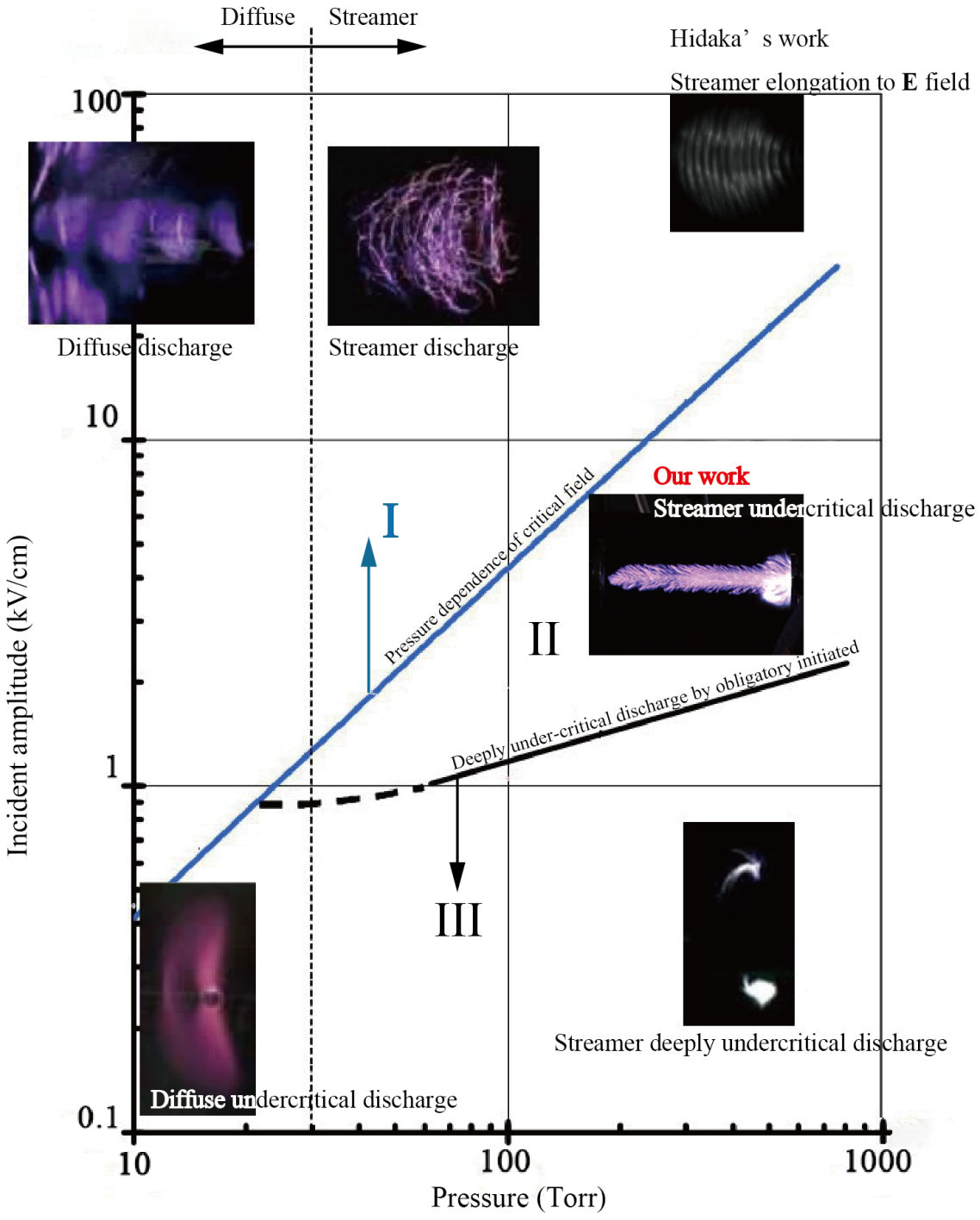

Figure 2-8 Classification of microwave discharge form [2, 27]

(Critical filed means “Paschen curve” in microwave range)

Therefore, we first tried to obtain the ionization frequency or attachment frequency from solving the kinetic equation. However this approach cannot estimate the ionization frequency or attachment frequency. This is because the results from the approach leads to the wrong value as the order of them are not correctly estimated. Hence, we decided to use the value of the attachment frequency and recombination coefficient according to[28]. About the ionization frequency, for the time being, we use an empirical fitting expression for the past experimental data.

The expression for the ionization frequency is typically of the form (2-77).

$$\frac{\nu_i}{p} = \frac{\nu_a}{p}\left[\left(\frac{E}{E_c}\right)^{\beta} - 1\right]. \tag{2-77}$$

Where p is ambient pressure and E_c is the critical field. β is the fitting parameter, and 5.3 is used in most of papers [29].

ν_a is given by [28]:

$$\nu_a = \alpha \cdot 1.1552 \cdot 10^7 \cdot \left(4.7 - 0.25\,E/N\right). \tag{2-78}$$

α is the fitting parameter. Usually α = 1, so we set it that value. Also, N is concentration of molecules in m^{-3}, and E_c is obtained from our experiments. At atmospheric pressure, E_c is almost 3.1kV/cm.

Recombination coefficient is given by [28]:

$$r_{ei} = \gamma \cdot 10^{-14} \cdot \left(300/T_e\right)^{1/2}\ \mathrm{m^3 s^{-1}}. \tag{2-79}$$

Also, γ is the fitting parameter. Usually γ= 0~1 have been used. We use γ= 1 as simulation condition.

3. Results and discussion

Recent simulations by Boeuf *et al* [7, 18] were reproduced at MIT [2, 3, 30]. In their work, the effective diffusion coefficient modeling was justified by comparing the simulation results with the 'more exact' drift diffusion Poisson model. Moreover, they also showed the influence of recombination coefficient and pressure and their 2D simulations in both (***E***, ***k***) plane and (***H***, ***k***) showed a good agreement in self-organized pattern formation comparing with the experimental result. The elongation of plasma filament formed in the standing wave at the intersection of two incident waves with opposed wave vectors and the front elongation to ***E*** field was successfully reproduced.

In our case we conducted 2D simulations in both (***E***, ***k***) plane and (***H***, ***k***) plane with the presence of many plasmoids in a cm-scale simulation domain like what we have done in the experiment. As a result, we found the tendency of the filament formation, and then we compared the simulation results of filamentary patterned and ionization front velocity with the experimental results. . Finally we discussed the mechanism of the ionization front propagation.

3.1 Calculation conditions

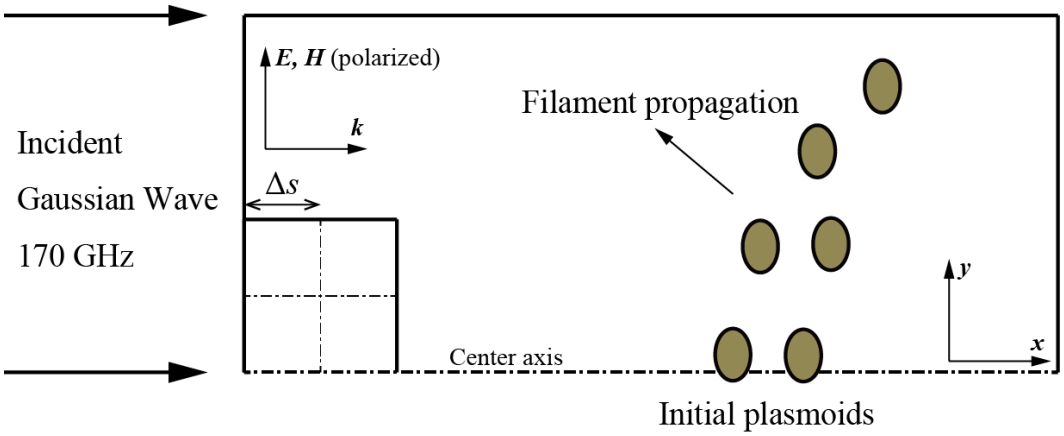

Figure 3-1 Schematic of the simulation domain

In this work, we performed the 2D simulation in two cases. In first case, the simulation plane (***x***, ***y***) contains ***H*** and the wave vector ***k*** (parallel to the ***x*** direction) while ***E*** is perpendicular to the plane. This case corresponds to the *x* and *z* direction as the wave direction and polarized plane respectively. In Boeuf's [7] and my cases, the filaments were perpendicular to the simulation plane and the stretching of the filaments did not appear in the simulation. In contrary, ***E*** and ***k*** were considered as the simulation domain while ***H*** is perpendicular instead for the second case. This case corresponds to a ***y***-polarized and ***x***-directed wave as shown in Figure 3-1. The filaments are in the simulation domain and the model showed the stretching of filament in the direction of the field as well as the propagation of the plasma toward the source which is similar to Boeuf *et al* [7].

The microwave frequency is 170 GHz (λ ~1.73 mm). The simulation domain is 2.5~ × 2.5~ λ, i.e., about 4.3~ × 4.3~ mm. In the experiment, the microwave beam was focused with a reflector which created 2 region of interested that are the near focal region and the almost steady region (region where the wave moves toward the source). In our simulation only the region where the ionization front propagation is almost steady was solved. In addition, the incident millimeter-wave beam did not set as the plane wave but the Gaussian wave. The equation is given by:

$$E(r,x) = E_0 \frac{w_0}{w(x)} \exp\left(\frac{-r^2}{w^2(x)} - ikx - ik\frac{r^2}{2R(x)} + i\varsigma(x) \right), \qquad (3\text{-}1)$$

where

r is the radial distance from the center axis of the beam,

x is the center axis, *i* is the imaginary unit,

$k=2\pi/\lambda$ is the wave number, E_0 is the amplitude at *x* at $w(x)= w_0$,

$w(x)$ is the radius at which the field amplitude and intensity drop to $1/e$ and $1/e^2$ of their axial values, respectively,

w_0 is the waist size (experimental condition : 2 cm),

$R(x)$ is the radius of curvature of the beam's wavefronts, and

$\zeta(x)$ is the Gouy phase shift, an extra contribution to the phase that is seen in Gaussian beams.

Additionally, the field has a time dependence factor $e^{i\omega t}$ which was used to suppress the above expression (3-1). The beam in the simulation is shown in Figure 3-2

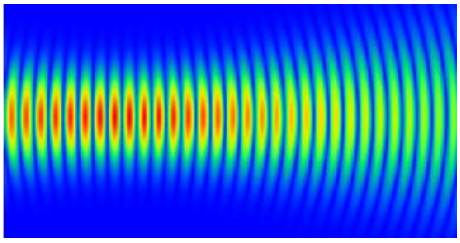

Figure 3-2 Incident Gaussian wave in the simulation

The initial electron density with a maximum of ~10^{22} m^{-3} was assumed in every simulation as shown in Figure 3-3. Different positions of the electron density have different value such that the initial plasma arrays changes with the simulations.

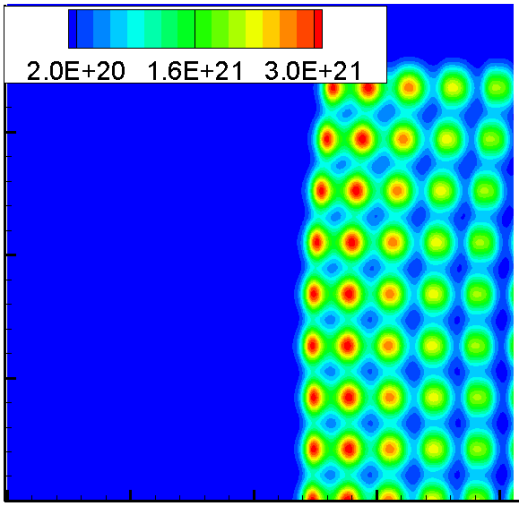

Figure 3-3 Initial electron density profile : n_e [m^{-3}]

3.2 Plasma formation in the domain to which E vector is perpendicular

According to the experimental conditions, we consider now a 170 GHz, 0.87 MV/m (0.2 MW/cm^2 in power density) wave at 760 Torr propagating from left to right along the x axis. When the $\boldsymbol{E}$ field is perpendicular to the simulation plane ($\boldsymbol{x}$, $\boldsymbol{y}$), i.e., ($\boldsymbol{H}$, $\boldsymbol{k}$) plane, the induced electron current in the plasma oscillates in the direction perpendicular to ($\boldsymbol{x}$, $\boldsymbol{y}$) and thus, the elongation of the filaments cannot be described in this configuration. This was also confirmed in Bueuf *et al*'s simulation [7, 18]. We will see in this section that the formation of an array of filaments can be described in the case of none single plasmoid as shown in Figure 3-4. So, we set the initial electron density as in Figure 3-4.

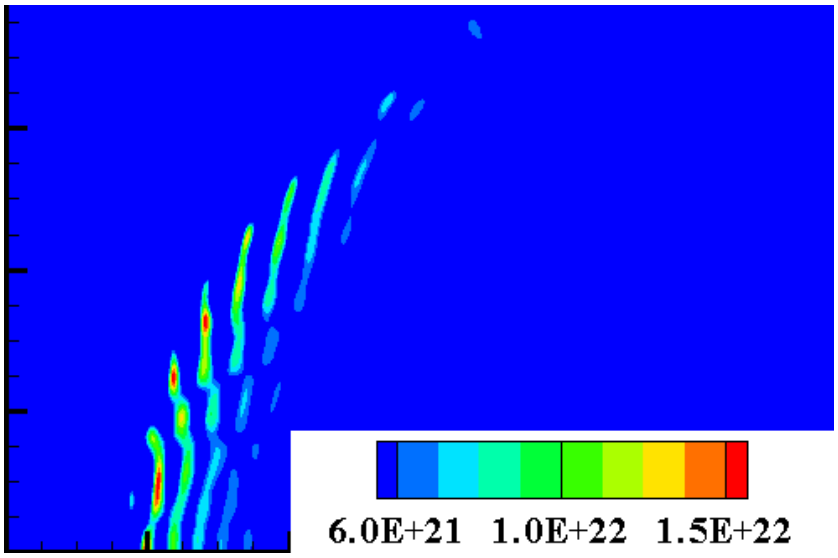

Figure 3-4 Initial electron density profile : n_e [m^{-3}]

Moreover, in this simulation we set α=1 and γ=1 in the source term modeling (2-79)-(2-81).

The time evolution of the plasma (electron) density is shown in Figure 3-5. The ionization front shape is bow-like and almost agrees with our experiments.

(a) t=40 nsec

: n_e [m^{-3}]

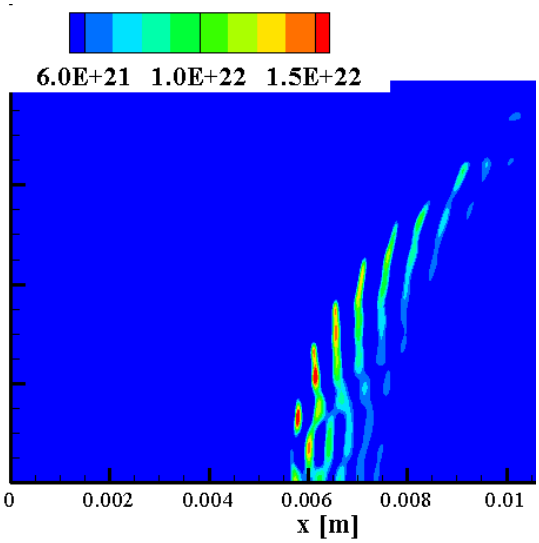

(b) t=70 nsec

: n_e [m^{-3}]

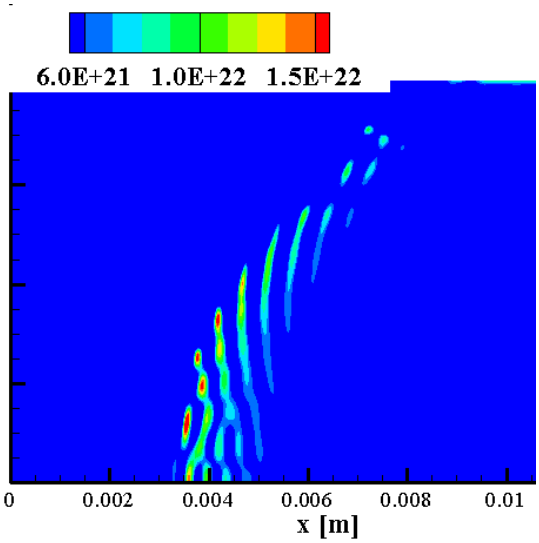

(c) t=100 nsec

: n_e [m^{-3}]

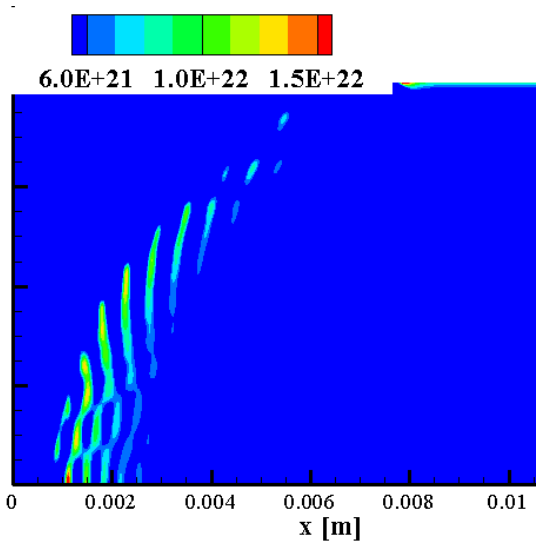

Figure 3-5 Time evolution of electron density

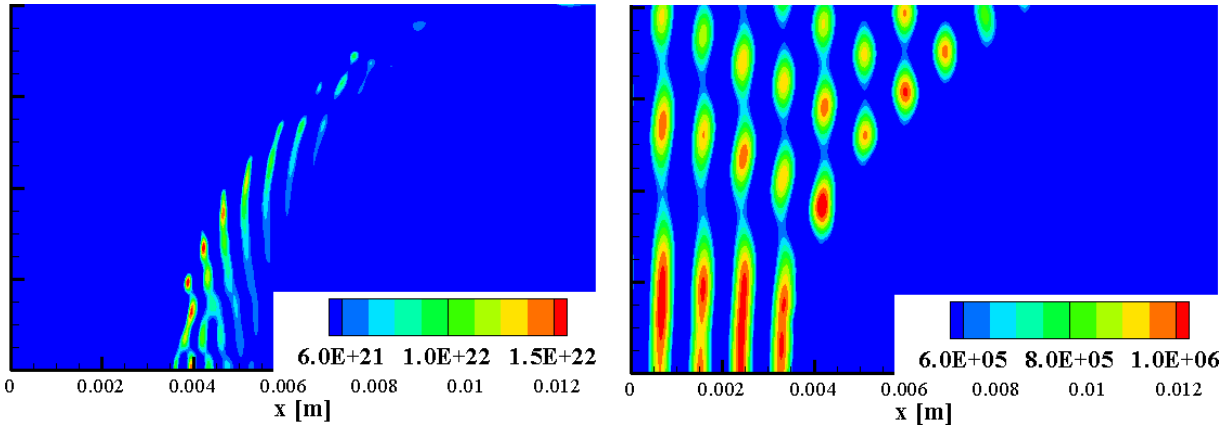

Figure 3-6 Plasma density distribution (left) : n_e [m^{-3}],

field intensity distribution (right) at a time-step : E_{rms} [V/m]

We can see from Figure 3-5 that the ionization front propagated into wave source. Moreover, from figure 3-6, the high intensity field was formed obliquely. And it is made of interference of the indent wave and the reflection by the interaction of the incident wave and plasmoids. Then in the high intensity region, new plasmoids were generated.

Here, we discuss the formation of the high intensity region in greater detail. Figure 3-7 shows the high intensity region at around center (y~0) region and the edge (y~1 cm) region.

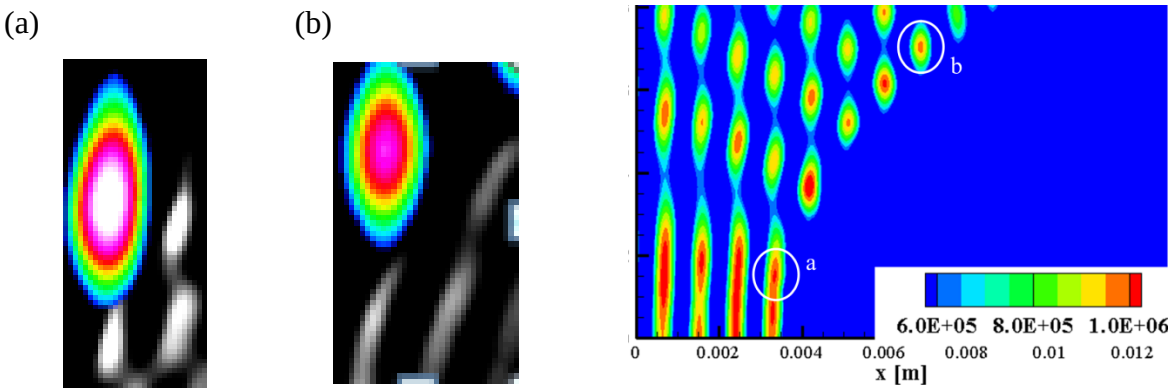

Figure 3-7 High intensity region (Rainbow scale) (a) :around center, (b) : in the edge,

grayscale shows electron density profile.

Right figure : typical field intensity distribution

In the center region, a plasmoid was generated between the plasmoids as shown in figure 3-7(a). Since in this region the electron density and the incident wave intensity do not vary with the distance from the center y~0. So, if two plasmoids was set such in figure 3-7(a), they caused comparable wave reflection from each plasmoid and then the high intensity field was generated in the position between the near plasmoids, resulting in the generation of plasma in the field. On the other hand, in the outer region (near the edge of the wave) plasma will be generated in the front of a plasmoid as shown in figure 3-7(b). In this region, field intensity became weaker toward away from the center axis because of Gaussian profile. This caused non-equivalent reflection. Thus instead of in between the plasmoids plasma was generated in front of the plasmoid itself. This difference leads to the different in propagation mechanism between the center region and the edge region. In the edge region, the ionization front propagated obliquely as described in Figure 3-8. This tendency agrees with our experiments.

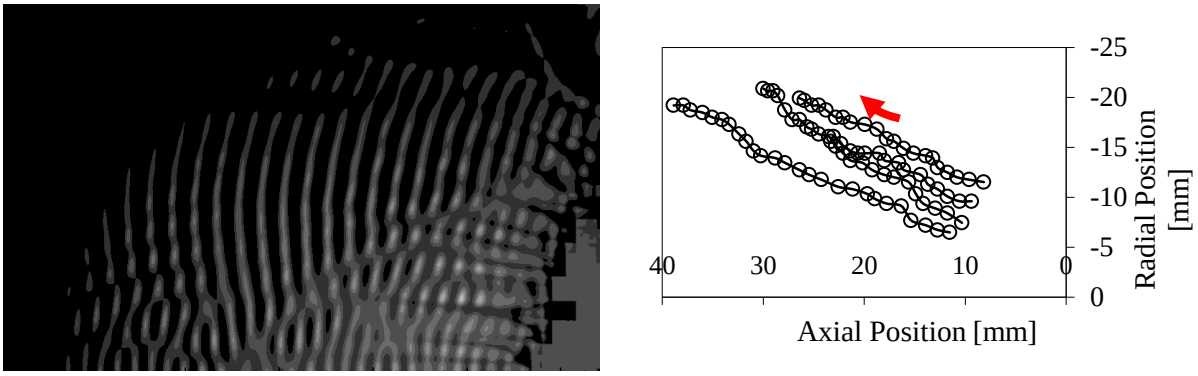

Figure 3-8 Left : Time integrated image of electron density,

Right : The trace of ionization front in experiments

However, the front velocity is much faster than our experiments. This is because our simulation scheme solved only one component in terms of electric field. Moreover ionization modeling is also attributed to this.

3.3 Plasma formation in the domain to which H vector is perpendicular

In this case we considered an incident 170 GHz plane wave with amplitude of 0.87 MV/m (0.2 MW/cm^2 in power density) at the atmospheric pressure (760 torr) propagating from left to right along *x*-axis. This condition is the same as section 3.2 condition. When the ***H*** field is perpendicular to the simulation plane (***x***, ***y***), i.e., (***E***, ***k***) plane, the induced electron current in the plasma oscillates in the direction parallel to (***x***, ***y***) and thus, the elongation of the filaments can be described in this configuration. This was also confirmed by Boeuf *et al*'s simulations [7, 18]. Furthermore, their simulations agreed with Hidaka's experiments (single plasmoid discharge) [2, 3]. Here, we conducted the simulations in the case of plasmoids just like the previous section.

In this simulation, we set α=1 and γ=1 in the source term modeling (2-79)-(2-81) as with the previous case.

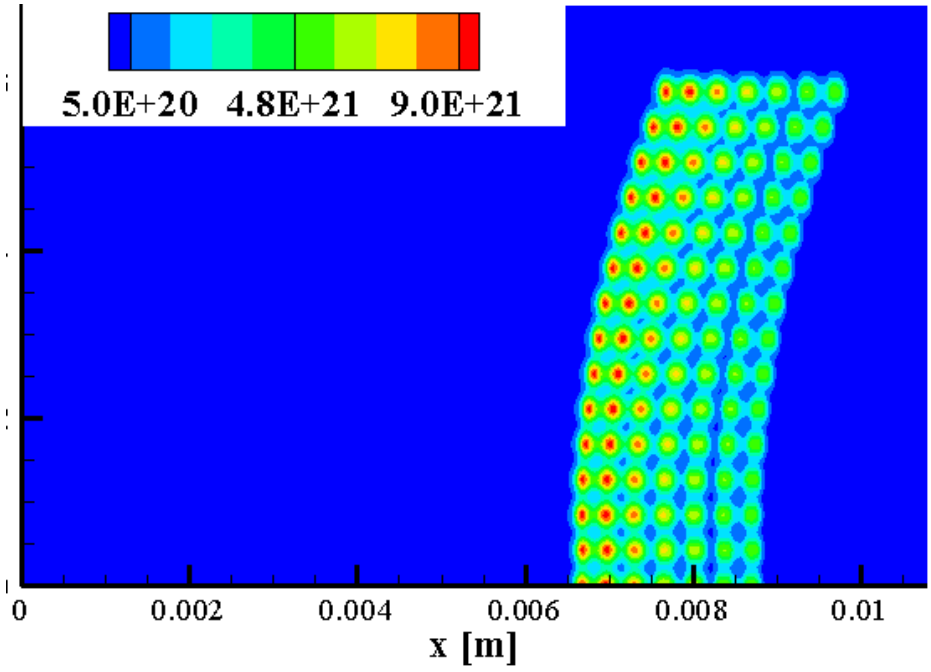

Figure 3-9 Initial electron density : n_e [m^{-3}]

The time evolution of the plasma (electron) density is shown in Figure 3-9. The ionization front propagated discretely in the *y* axis. This hasn't been found in our experiments.

t=140 nsec

: n_e [m^{-3}]

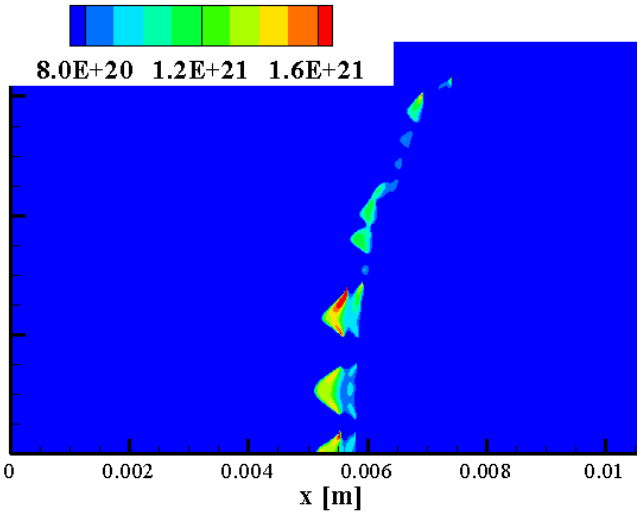

t=250 nsec

: n_e [m^{-3}]

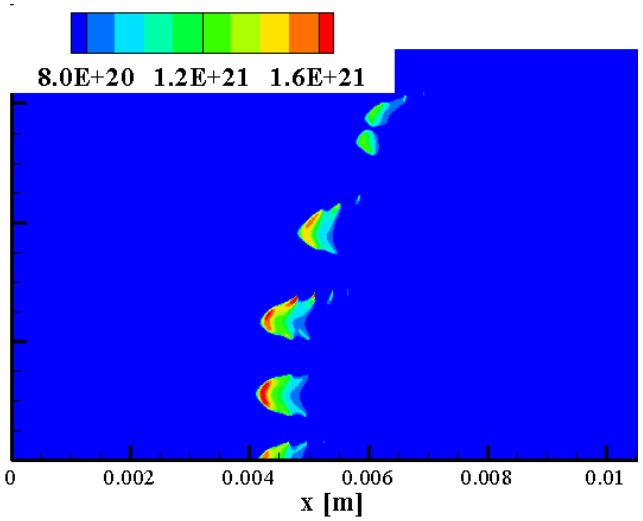

t=390 nsec

: n_e [m^{-3}]

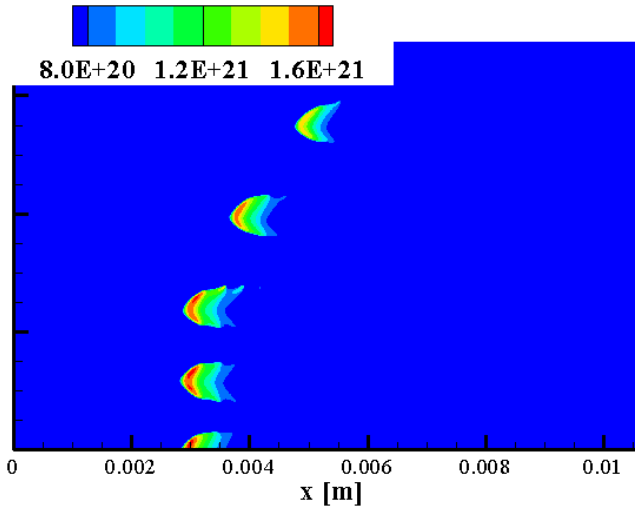

Figure 3-10 Time evolution of electron density

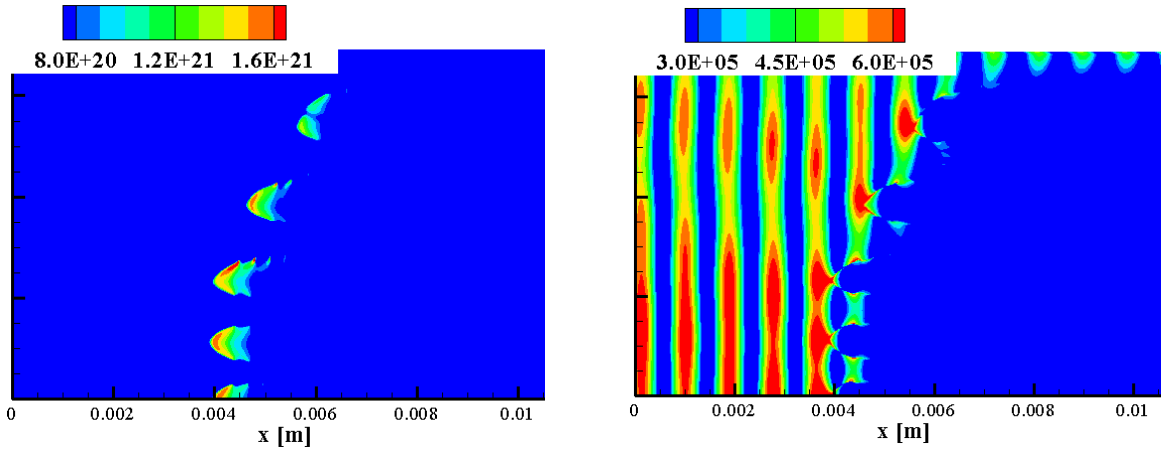

Figure 3-11 Plasma density distribution (left) : n_e [m^{-3}],

field intensity distribution (right) at a time-step : E_{rms} [V/m]

We can see from Figure 3-10, ionization front itself propagated into the wave source. Moreover, from figure 3-10, the high intensity field was formed obliquely in a whole. However, the ionization front did not propagate obliquely but parallel with *x* axis. This is because high intensity field near plasmoids was formed in the front of a plasmoid shown in figure 3-12.

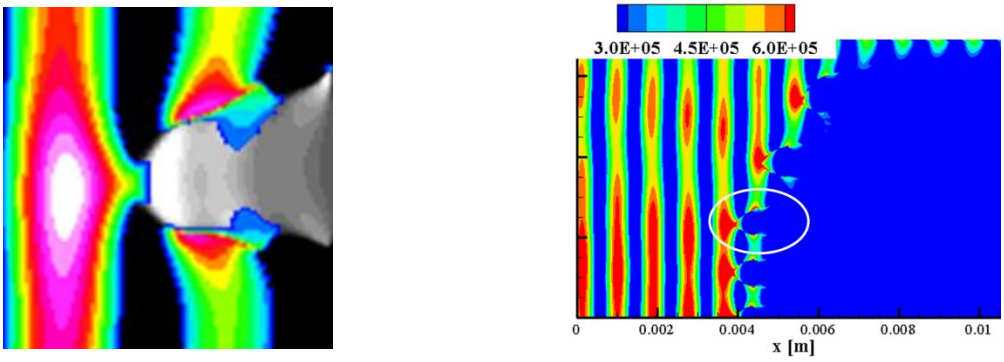

Figure 3-12 High intensity region (Rainbow scale), grayscale shows electron density profile.

Right figure (white circle shows left figure): typical field intensity distribution

This interaction that was formed the filed in the front of a plasmoid was caused by plasma elongation to the ***E*** field. Thus, the time of interaction between the incident wave and the reflection wave was lengthened by this elongation. .Accordingly, it can be considered that high intensity field was dragged from the original (oblique) position to the front of a plasmoid.

Similarly, the ionization front velocity was higher than the experimental value because of the same reason as already mentioned in the previous case.

3.4 The velocity and structure of the plasma front

3.4.1 Modifying of ν_i and ν_a for Tokyo University experiments

As mentioned above, the time averaged velocity of the ionization front was found to be around 10 km/s in (***E***, ***k***) plane and much faster in (***H, k***) plane, which it is obviously that there is a huge difference compare to the experimental value. As the ionization front velocity in the experiment at atmospheric pressure was about 100m/sec~1 km/sec as shown in in Figure 3-13.

This is because the empirical equation of the ionization and attachment frequency (2-79), (2-80) was overestimated on the order of themselves. When the expression was used, the front velocity was estimated to be around 6 km/sec from the "theoretical" speed $U_{\text{ion}} = \sqrt{2D_e\nu_i}$ [16, 17]. However, we don't actually have the experimental data or any calculation of the ionization or the attachment coefficients in our bean's power range. Since the past studies did not include the power range we used because of under-critical field but on the other hand the source term is very important for reproducing our experiments.

Then, in turn, we deduced the ionization and attachment frequency from $U_{\text{ion}} = \sqrt{2D_e\nu_i}$ to suit our experimental velocity in Figure3-13 (fitting). Then we used four following expressions (3-2)-(3-5) and also we did the fitting. The expressions are given by:

Ionization frequency
$$\frac{\nu_i}{p} = \frac{\nu_a}{p}\left(\frac{E_{\text{rms}}}{E_{\text{cr.}}}\right)^{\beta},\ E_{\text{cr.}}:\text{Critical field},\qquad (3\text{-}2)$$

Attachment frequency[28]
$$\nu_{\text{a}} = \alpha(4.7 - 0.25 f(E_{\text{rms}}))N_{\text{air}}^2,\qquad (3\text{-}3)$$

Diffusion coefficient
$$D_e = \mu_e \frac{kT_e}{e} = \frac{e}{m_e\nu_m}\frac{kT_e}{e},\qquad (3\text{-}4)$$

Electron temperature [31]
$$\frac{kT_e}{e} = \left[2.1\times10^{-5}\frac{E_{\text{rms}}}{p}\left(91+\frac{E_{\text{rms}}}{p}\right)\right]^{1/3}.\qquad (3\text{-}5)$$

The first expression can be taken from the empirical expression. The second expression is taken from Kossyi *et al's* [28] calculation fitting. Diffusion coefficient is deduced from the Einstein's relations. Electron temperature is as reference with Woo *et al's* [31] relation.

At first, we selected the diffusion coefficient from (3-4) and (3-5) equations in our power range. Next, we assumed the critical field $E_{cr.}$from our experiments. Finally, we decided to choose the ionization and attachment frequency from (3-2) and (3-3) equations in order to reproduce experimental ionization front velocity's characteristics as shown in Figure 3-13. Thus, it is possible to reproduce the plasma pattern in our experimental range (low power density). In the new expressions, we set α=0.008, β=4.1in (3-2)-(3-3).

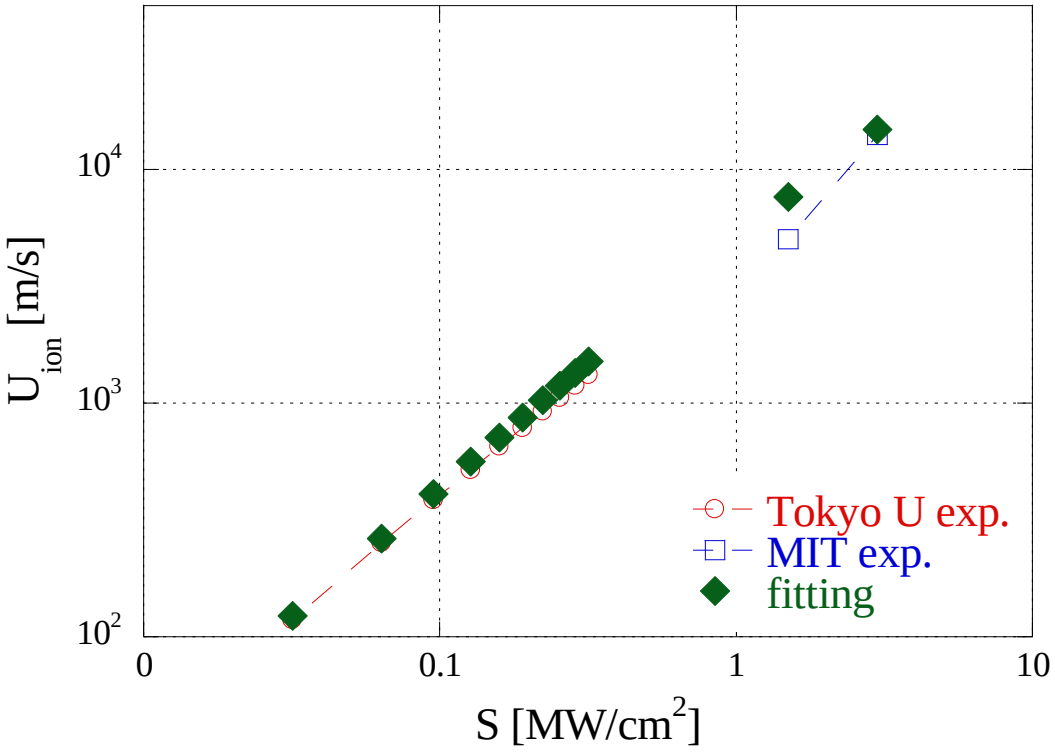

Figure 3-13 Ionization front velocity as function of beam's peak power density at 760 Torr [2]

As we mentioned before, the ionization front velocity is different in (***E***, ***k***) and (***H***, ***k***) plane. This is because our simulation scheme has solved only one component of an electric field in (***H***, ***k***) plane and two components in (***E***, ***k***) plane. Hence, it is possible to say that the

value of front velocity in (***E***, ***k***) plane is closer to the accurate value. As a result, we conducted the simulation in (***E***, ***k***) plane for the velocity's comparison.

3.4.2 Ionization front propagation in our experimental power region

First, we simulated the ionization front propagation in our experimental conditions. Figure 3-14 shows electron density distribution in (***E***, ***k***) plane at some time step. We also showed the time development of the ionization front in the surrounded region of Figure 3-14 with white dashed line.

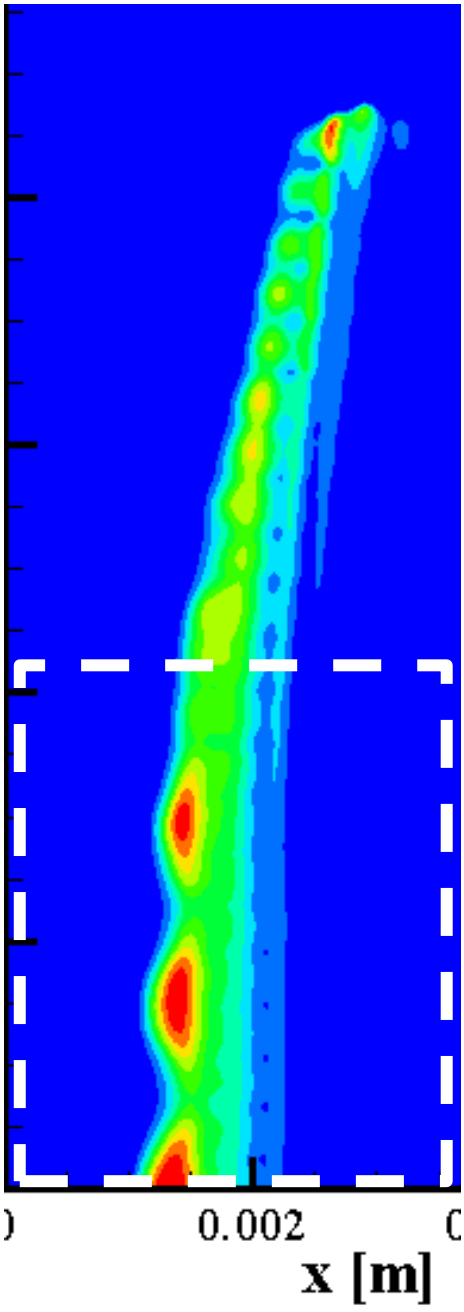

Figure 3-14 Ionization front at some time step

n_e [m^{-3}] :

t=1200 nsec

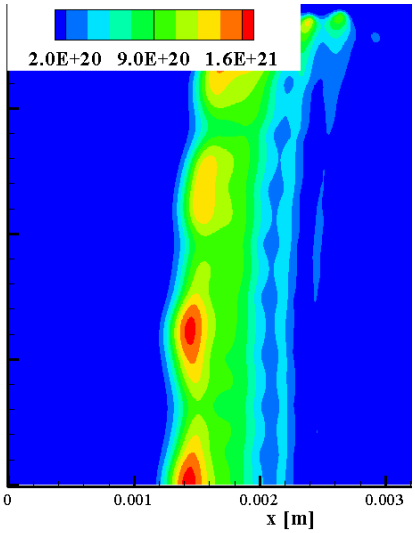

n_e [m^{-3}] :

t=1600 nsec

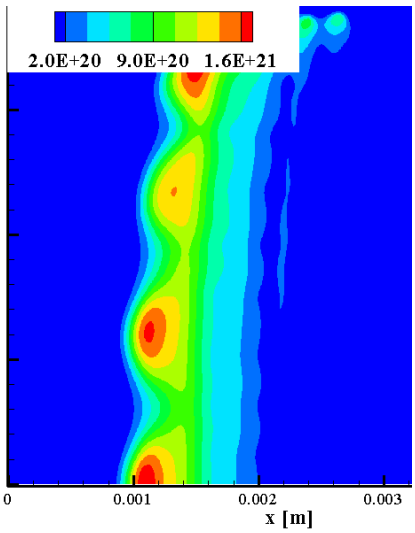

n_e [m^{-3}] :

t=1900 nsec

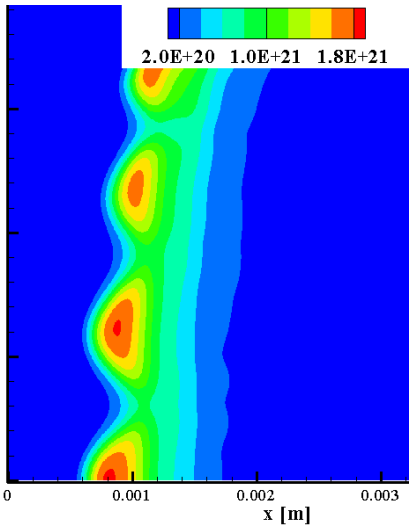

Figure 3-15 Time-development of ionization front in our experimental conditions

3.4.3 Ionization front propagation in MIT experimental power region

In addition, we simulated the ionization front propagation in MIT experimental conditions. Figure 3-16 shows electron density distribution in (***E***, ***k***) plane at some time step. Similarly, we then showed the time development of the ionization front in the surrounded region of Figure 3-16with white dashed line.

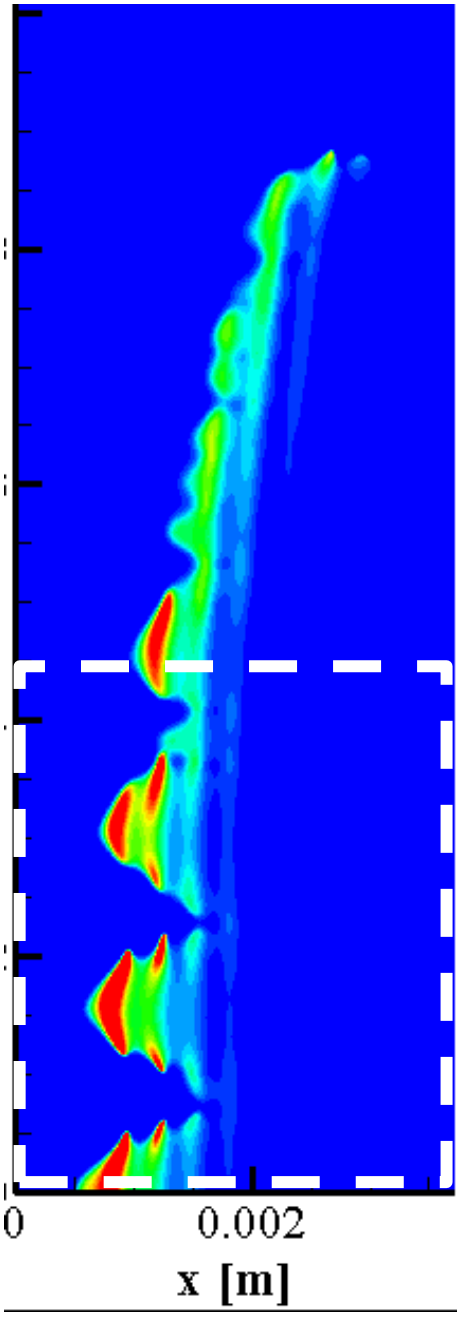

Figure 3-16 Ionization front at some time step

n_e [m^{-3}] :

t= 67 nsec

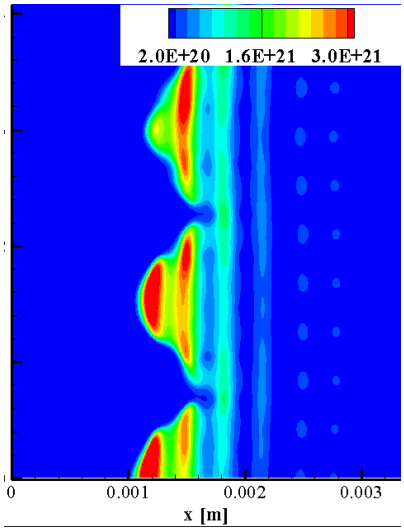

n_e [m^{-3}] :

t=105 nsec

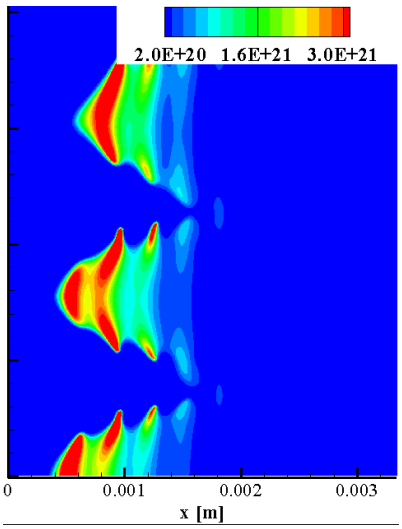

n_e [m^{-3}] :

t=132 nsec

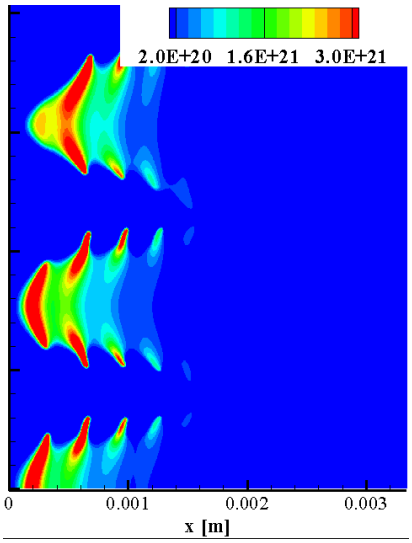

Figure 3-17Time-development of ionization front in MIT experimental conditions

3.4.4 Discussion

We can see from these figures that the plasma front propagated into the wave source in both cases, but the plasma pattern is obviously different as shown in Figure 3-18. In high power density region, we can see from the right hand side of Figure 3-18 that the structure is characterized by the streamer and discrete. On the other hand, in the left hand side, the structure is characterized by non-streamer and non-discrete.

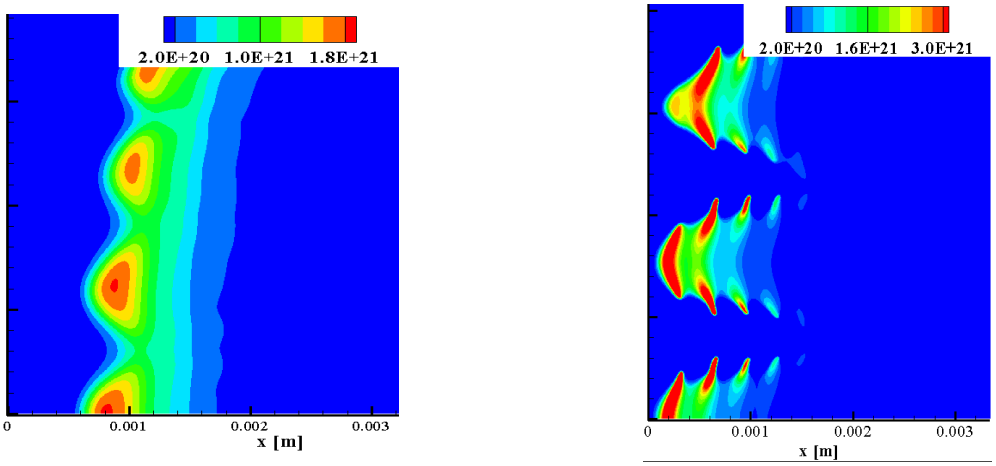

Figure 3-18 Ionization front structure in low power (left) and high power (right)

About the front velocity in the simulations, we obtain some agreements with the experiments. The comparison is shown in Figure 3-19.

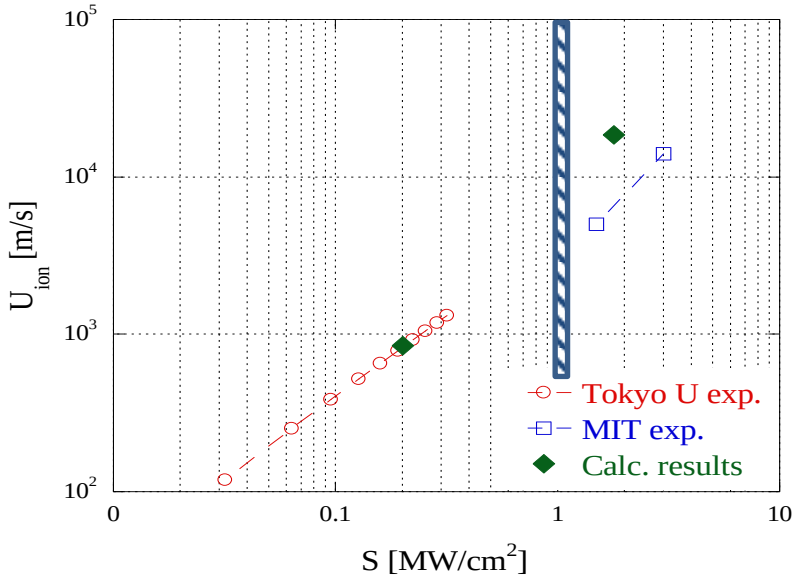

Figure 3-19 Ionization front velocity in simulations and experiments [2]

In case of plasma pattern, especially streamer, a past study [5] said that there is a boundary of beam power density which transits into streamer propagation. In Figure 3-19 (transverse line), the boundary is about 1~1.2 MW/cm^2 at atmospheric pressure. According to the study, if the beam power density is over the boundary value, the streamer structure can be seen. However, if the power density is below the boundary value, the streamer structure doesn't show up. This experimental tendency agrees with our simulation as shown in figure 3-18. This characteristic can be discussed by the relation between the diffusion coefficient and the ionization frequency. This can be explained by the "theoretical" speed $U_{\text{ion}} = \sqrt{2D_e \nu_i}$. The diffusion coefficient does not almost change by beam power density, but the ionization frequency is drastically changing. So, in the case of low power range, it is possible to deduce the effect of the electron diffusion such that it becomes greater than in the case of high power condition. It can be considered that this makes the plasma pattern changes.

As a result, in (***E***, ***k***) plane, we can suggest that there is a boundary which causes the filamentary to form.

4. Conclusions

The formation of a self-organized plasma array and its propagation toward to the source during high pressure air breakdown by a linear polarization 170 Gaussian wave was investigated using a 2D plasma-Maxwell's model in this thesis. The comparison between the simulation results and the experimental results at JAEA (Japan Atomic Energy Agency) was conducted to investigate the pattern structures and plasma front propagation velocities.

Followings are the conclusion

1. According to the simulation results, we can see that either in (***H***, ***k***) or (***E***, ***k***) domain, the ionization front propagated toward the wave source.

2. In (***H, k***) domain, the ionization front propagated obliquely in the region far from the center region of the Gaussian wave profile.

3. In (***E, k)*** domain, the ionization front propagated in the direction of the wave itself i.e. parallel to the ***k*** direction**.** This phenomenon occurred due to the front elongation to the E field

4. In case of the original ionization term, we found that the front velocity is comparatively faster than the experimental value. In contrast, if we used the modified ionization term, the value from simulation agreed with the value from the experiment. Moreover, this agreement includes the plasma filamentary structure as it became blob-like which is similar to the experimental result.

Bibliography

[1] H. Katsurayama, K. Komurasaki and Y. Arakawa, "'A preliminary study of pulse-laser powered orbital launcher," *Acta Astronaut.*, vol. 65, no. 7-8, OCT-NOV 2009, pp. 1032-1041.

[2] Y. Hidaka, E.M. Choi, I. Mastovsky, M.A. Shapiro, J.R. Sirigiri, R.J. Temkin, G.F. Edmiston, A.A. Neuber and Y. Oda, "'Plasma structures observed in gas breakdown using a 1.5 MW, 110 GHz pulsed gyrotron," *Phys Plasmas*, vol. 16, no. 5, MAY 2009, pp. 055702.

[3] Y. Hidaka, E.M. Choi, I. Mastovsky, M.A. Shapiro, J.R. Sirigiri and R.J. Temkin, "'Observation of large arrays of plasma filaments in air breakdown by 1.5-MW 110-GHz gyrotron pulses," *Phys.Rev.Lett.*, vol. 100, no. 3, JAN 25 2008, pp. 035003.

[4] P.V. Vedenin and N.A. Popov, "'Propagation of a high-pressure microwave discharge in prebreakdown fields: Formation of plasma structures," *Journal of Experimental and Theoretical Physics*, vol. 96, no. 1, 2003, pp. 40-52.

[5] V.G. Brovkin, "'Structure and dynamics of stimulated microwave gas discharge in wave beams," *Journal of the Moscow Physical Society*, vol. 5, no. 1, pp. 23-38.

[6] Y. Oda, K. Komurasaki, K. Takahashi, A. Kasugai and K. Sakamoto, "'Plasma generation using high-power millimeter-wave beam and its application for thrust generation," *J.Appl.Phys.*, vol. 100, no. 11, DEC 1 2006, pp. 113307.

[7] J. Boeuf, B. Chaudhury and G.Q. Zhu, "'Theory and Modeling of Self-Organization and Propagation of Filamentary Plasma Arrays in Microwave Breakdown at Atmospheric Pressure," *Phys.Rev.Lett.*, vol. 104, no. 1, JAN 8 2010, pp. 015002.

[8] G. Mur, "'Absorbing Boundary-Conditions for the Finite-Difference Approximation of the Time-Domain Electromagnetic-Field Equations," *IEEE Trans.Electromagn.Compat.*, vol. 23, no. 4, 1981, pp. 377-382.

[9] J.T. Mayhan, "'Comparison of various Microwave Breakdown Prediction Models," *J.Appl.Phys.*, vol. 42, no. 13, 1971, pp. 5362-&.

[10] W.P. Allis and D.J. Rose, "'The Transition from Free to Ambipolar Diffusion," *Physical Review*, vol. 93, no. 1, 1954, pp. 84-93.

[11] S.K. Nam and J.P. Verboncoeur, "'Theory of Filamentary Plasma Array Formation in Microwave Breakdown at Near-Atmospheric Pressure," *Phys.Rev.Lett.*, vol. 103, no. 5, JUL 31 2009, pp. 055004.

[12] I.P.(.P. Raĭzer, "'Gas discharge physics / Yuri P. Raizer,", 1991.

[13] D. Anderson, M. Lisak and T. Lewin, "'Self-Consistent Structure of an Ionization Wave Produced by Microwave Breakdown in Atmospheric Air," *Phys.Fluids*, vol. 29, no. 2, FEB 1986, pp. 446-449.

[14] H. Hamnen, D. Anderson and M. Lisak, "'A Model for Steady-State Breakdown Plasmas in Microwave Transmit-Receive Tubes," *J.Appl.Phys.*, vol. 70, no. 1, JUL 1 1991, pp. 93-98.

[15] J. Meunier, P. Belenguer and J.P. Boeuf, "'Numerical-Model of an Ac Plasma Display Panel Cell in Neon-Xenon Mixtures," *J.Appl.Phys.*, vol. 78, no. 2, JUL 15 1995, pp. 731-745.

[16] U. Ebert, W. vanSaarloos and C. Caroli, "'Propagation and structure of planar streamer fronts," *Physical Review E*, vol. 55, no. 2, FEB 1997, pp. 1530-1549.

[17] U. Ebert, W. vanSaarloos and C. Caroli, "'Streamer propagation as a pattern formation problem: Planar fronts," *Phys.Rev.Lett.*, vol. 77, no. 20, NOV 11 1996, pp. 4178-4181.

[18] B. Chaudhury and J. Boeuf, "'Computational Studies of Filamentary Pattern Formation in a High Power Microwave Breakdown Generated Air Plasma," *IEEE Trans.Plasma Sci.*, vol. 38, no. 9, SEP 2010, pp. 2281-2288.

[19] K.S. Yee, "'Numerical Solution of Initial Boundary Value Problems Involving Maxwells Equations in Isotropic Media," *Ieee Transactions on Antennas and Propagation*, vol. AP14, no. 3, 1966, pp. 302-&.

[20] K.S. Kunz and R.J. Luebbers, "'The finite difference time domain method for electromagnetics / Karl S. Kunz, Raymond J. Luebbers,", 1993.

[21] G. Mur, "'Total-field absorbing boundary conditions for the time-domain electromagnetic field equations," *IEEE Trans.Electromagn.Compat.*, vol. 40, no. 2, MAY 1998, pp. 100-102.

[22] K.L. Shlager and J.B. Schneider, "'Selective Survey of the Finite-Difference Time-Domain Literature," *Ieee Antennas and Propagation Magazine*, vol. 37, no. 4, AUG 1995, pp. 39-57.

[23] 恵 蒋, "'不等間隔メッシュを用いた FDTD 法によるモノポールアンテナの解析," *電子情報通信学会技術研究報告.A・P, アンテナ・伝播*, vol. 98, no. 46, pp. 7-12.

[24] S.A. Cummer, "'An analysis of new and existing FDTD methods for isotropic cold plasma and a method for improving their accuracy," *Ieee Transactions on Antennas and Propagation*, vol. 45, no. 3, MAR 1997, pp. 392-400.

[25] S.J. Huang, "'Exponential time differencing FDTD formulation for plasma," *Microwave Opt Technol Lett*, vol. 49, no. 6, JUN 2007, pp. 1363-1364.

[26] A.D. MacDonald, "'Microwave breakdown in gases / [by] A.D. MacDonald,", 1966.

[27] K.V. Khodataev, "'Microwave discharges and possible applications in aerospace technologies," *J.Propul.Power*, vol. 24, no. 5, SEP-OCT 2008, pp. 962-972.

[28] I.A. Kossyi, A.Y. Kostinsky, A.A. Matveyev and V.P. Silakov, "'Kinetic scheme of the non-equilibrium discharge in nitrogen-oxygen mixtures," *Plasma Sources Science & Technology*, vol. 1, no. 3, AUG 1992, pp. 207-220.

[29] G.Q. Zhu, J. Boeuf and B. Chaudhury, "'Ionization-diffusion plasma front propagation in a microwave field," *Plasma Sources Science & Technology*, vol. 20, no. 3, JUN 2011, pp. 035007.

[30] A. Cook, M. Shapiro and R. Temkin, "'Pressure dependence of plasma structure in microwave gas breakdown at 110 GHz," *Appl.Phys.Lett.*, vol. 97, no. 1, JUL 5 2010, pp. 011504.

[31] W. Woo and J.S. Degroot, "'Microwave-Absorption and Plasma-Heating due to Microwave Breakdown in the Atmosphere," *Phys.Fluids*, vol. 27, no. 2, 1984, pp. 475-487.

[32] Guo-qiang ZHU, "'Modeling of plasma dynamics and pattern formation during high pres-suremicrowave breakdown in air," *Doctoral thesis*, 2012

Works

国内学会

1. 武市天聖，山口敏和，福成雅史，小紫公也，小泉宏之，荒川義博，“ミリ波駆動デトネーションの伝播速度制御によるマイクロ波ロケット推進性能の向上”，第 55 回宇宙科学技術連合講演会，松山，2011 年 12 月

2. 武市天聖，山口敏和，福成雅史，小紫公也，荒川義博，“大気圧ミリ波放電における電離波面形成過程の数値解析”，第 43 期年会講演会，東京大学，2012 年 4 月

International conference

1. Tensei Takeichi, Toshikazu Yamaguchi, Masafumi Fukunari, Hiroyuki Koizumi, Kimiya Komurasaki, Yoshihiro Arakawa, “Numerical studies of filamentary plasma formation in high power millimeter wave field”, The 65th Gaseous Electronics Conference, TX AUS, Oct. 2012

2. Tensei Takeichi, Toshikazu Yamaguchi, Masafumi Fukunari, Hiroyuki Koizumi, Kimiya Komurasaki, Yoshihiro Arakawa, “Modeling of oblique ionization front propagation in high power millimeter wave field”, Division of Plasma Meeting 2012, PVD RI, Nov. 2012